Challenge Journal of STRUCTURAL MECHANICS

Vol.4 No.3 (2018)

buckling building codes columns continuous girder bridge durability dynamic analysis dynamic response earthquake finite element analysis finite element method meridional stresses operational modal analysis optimization reinforced concrete seismic analysis seismic design seismic isolation seismic response shallow foundations smart concrete teaching-learning based optimization

ISSN 2149-8024

TULPAR ACADEMIC PUBLISHING

Challenge Journal of Structural Mechanics

E-mail: *cjsmec@challengejournal.com*

Web page: *cjsmec.challengejournal.com*

TULPAR Academic Publishing
www.tulparpublishing.com

Challenge Journal of Structural Mechanics

CONTENTS

Research Articles

TULPAR ACADEMIC PUBLISHING

Challenge Journal of Structural Mechanics

Research Article

Re-examination of steel frame office buildings in preventing collapse when subject to intense fires

Robert Korol *, Ken Sivakumaran, Paul Heerema

Department of Civil Engineering, McMaster University, Hamilton, Ontario L8S 4L7, Canada

ABSTRACT

The purpose of the paper is to investigate the extent to which present-day design of steel framed buildings is susceptible to total collapse when subjected to extreme fire events. We select a 50 storey structure in which 2 and 4 adjacent storeys located at different above-ground heights are, in separate scenarios engulfed in raging fires. A total of 8 scenarios are analyzed, employing Newtonian mechanics and realistic energy dissipating properties of H-shaped columns and normal concrete floor slabs possessing secondary (shrinkage and temperature) reinforcement alone. While the present Canadian building code is the basis for our column designs, other standards provide very similar specifications. Although fire proofing is required in virtually all high rise building construction, we are excluding such materials in order to simplify the analyses, but clearly do not advocate its omission – quite the opposite in fact. As well, attributes such as floor beams, partitions and furnishings of every description, all of which would in practice participate in absorbing the kinetic energy of a crush-down upper block are excluded. Despite such a vast array of conservative assumptions, it is shown that partial collapse may occur during crush-down, however, in no case will total collapse be the consequence. These results should provide some comfort to code writers that their requirements should indeed prevent the most catastrophic of failures due to fires.

ARTICLE INFO

Article history:
Received 7 December 2017
Revised 20 March 2018
Accepted 2 June 2018

Keywords:
Hi-rise steel frame buildings
Fire events
Energy dissipation elements
H-shaped columns
Secondary reinforced concrete floors
Newtonian mechanic principles
Collapse states

1. Introduction

Prior to the horrendous events of 9/11 that resulted in thousands of deaths and the total destruction of three high rise steel framed buildings in the World Trade Center complex in New York City, the issue of fires being the cause of collapse of such structures was ignored for good reason. An excellent earlier history of fire safety inferred that existing fire protection of the supporting structure together with life safety systems were indeed sufficient. Even the authors of the FEMA 403 report (2002) concluded that no significant changes were warranted in building codes and design practice. The circumstances of that day in 2001 were deemed to be an extraordinary combination of extreme events that could not have been anticipated**.**

Surprisingly, perhaps, is the huge number of fire events that occur in high rise buildings every year that are generally unreported because of the rarity of associated collapse events. For example, John Hall Jr. has published reports for the National Fire Protection Association in the U.S. (2001, 2013) that provide statistics showing, on average, 10,000 significant fires having occurred annually in buildings 7 storeys or more in periods 1985-1998 and 2007-2011 respectively, with occupancy classifications being: apartments, hotels and motels, hospitals and care facilities, and offices. Although the latter 5 year period reveals somewhat fewer fire events than the earlier study, that data, together with the events of 9/11 have inspired the structural engineering profession to devote greater efforts to reduce the risks of fire, civilian deaths and injuries and property damage. In that regard,

* *Corresponding author*. Tel.: +1-905-525-9140 ; Fax: +1-905-529-9688 ; E-mail address: korol@mcmaster.ca (R. Korol)
ISSN: 2149-8024 / DOI: https://doi.org/10.20528/cjsmec.2018.03.001

a very comprehensive, but difficult to verify computer model known as the Fire Dynamics Simulator (FDS) which purportedly "gave good agreement with the fire spread as observed at the windows" of WTC 1 and 2 (McAllister et al., 2013), but when later improvements were made to FDS, attempts to confirm its validation for reconstructing the magnitude of the WTC fires was described as weak (Quintiere and Williams, 2014).

Engineers and scientists who have a rudimentary knowledge of structural design and thermal properties of materials should not be expected to accept on faith the results of computer analyses, especially when they are at odds with historical data, as were the circumstances involving the demise of the WTC towers. In an earlier paper on the collapse of WTC7 (Korol et al.,2015), we undertook a fire analysis that accounted for fire loadings and temperature-time plots to ascertain if that structure could have succumbed by fire alone. However, in this article, our purpose is to undertake a simplified analysis that accepts worst case conditions on a generic steel framed 50 storey office building weakened by fire loadings, employing conventional principles of engineering design and Newton's laws, and to which gravity loads are applied. In this regard, a series of 8 scenarios will be examined involving adjacent 2 and 4 storey fires at levels ranging in 10 storey increments from top to bottom - the objective being to assess the extent to which partial or total collapse would be the result.

2. Description of the Postulated Structure

We begin by assuming a rectangular-shaped 50 storey hi-rise office building, having equal storey heights of 4m for which non-core areas (our focus) occupy an area of 3,920 m^2. For purposes of simplicity, we assume a regular grid consisting or 80 equal sized columns in a given storey, a segment of which is noted in Fig. 1, with tributary areas of 49 m^2 and sizes commensurate with gravity loading based on load and resistance factors consistent with the most recent design code for steel structures used in Canada (CSA, 2014). It's assumed that W-shapes are employed for the columns with size changes occurring in three storey segments. A commonly-used series in such applications is W360 which has a wide range of weights and dimensions compatible as columns in compression load transfer, with upper column footprints contained within the cross section profiles consistent with those below. This form of column stacking provides for simplified and cost efficient detailing for which splice and filler plates alone are needed for full moment and shear transfer compatibility.

It will be assumed that the steel is construction grade, having a nominal yield stress value, F_y of 345 MPa, which will be reduced to a value defined as F_y^* to account for compressive loading of slender elements in compression (flanges and web) in accordance with the Canadian design code mentioned earlier. As well, there is the matter of selecting column sizes to minimize fabrication costs (i.e. choosing sections that are continuous for 3 storeys). For Scenario 1, we assume a constant size for columns occupying the uppermost storeys for which fires will rage, i.e. the 40th and 41st levels. A design computation for sizing these columns must therefore be based on prescribed loadings on various floors, for which we chose the 40th for our example that also must take into account column slenderness. A detailed computation for this case is presented in Appendix A.

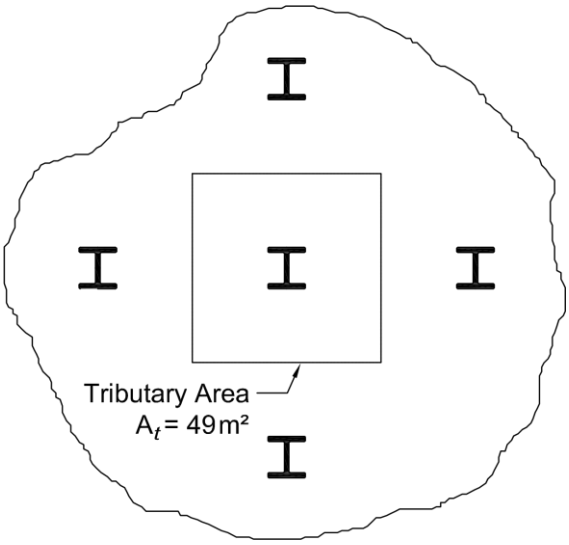

Fig. 1. Non-core column arrangement.

Meanwhile, the floors at all levels and the factored gravity loading appropriate at that level are presumed to consist of normal strength concrete having an average thickness of 102 mm (4") and containing wire mesh, ostensibly cast onto ribbed steel deck, meant to resist shrinkage and temperature cracks. Although the floors will obviously require floor beams and girders to support floor loadings, our analysis will ignore the twisting and bending energy absorbed during a potential global collapse event. In this way, we are assured that actual collapse states will be less severe than what we predict from our analysis.

3. Assumptions Associated with Collapse Initiation

In the design of any structure, a reasonable margin of safety is needed that accounts both for unanticipated overload conditions, and a possible strength deficiency of the material below its nominal value. In general, a high overload value, generally above 3 is the norm when lateral loads from winds and earthquake are present.

However, for our case, we will assume that the core of the structure will contain the elevator shaft, stairwells and mechanical rooms with a reinforced concrete perimeter wall which, together with robust steel columns provides the structural system needed to resist lateral loading. In the non-core area therefore, we assume that resistance to gravity loading alone controls the design of the columns based on limit states. The safety factor then represents a ratio of the factored gravity loads divided by realistic load values existing under the situation of a fire event. The resistance factor for the columns, therefore, is based on both the nominal steel strength and an

effective length factor for equally loaded columns at given floor levels. Even discounting the bending restraint provided by floor beams and girders, a factor of safety of approximately 2 is provided based on industry standards and noted by Wikipedia which states "Design factors for specific applications are often mandated by law, policy, or industry standards. Buildings commonly use a factor of safety of 2.0 for each structural member. The value for buildings is relatively low because the loads are well understood and most structures are redundant." General details are noted under "Wikipedia" in our References section. A further breakdown of loads and resistance information is presented in Appendix A for the case described as Scenario 1. As noted, fires raging throughout a given storey will reduce column strength equally to all columns, but for computational purposes, the equivalent of 39 of the 80 columns fail totally, thus offering no further resistance. Consequently, we make the assumption that 41 remain with full load capacity and which will offer resistance at the instant that collapse of the upper block is initiated. This value represents an average, since column sizes are limited and can only provide approximate factors of safety for given storeys. Overall, however, this number is on the conservative side in virtually all design situations and as such is the value which we shall ascribe to our design example.

Such a value will be presumed to mean that the equivalent of slightly more than 50% of the columns in a storey that is fully ablaze are able to resist the loads above it until progressive collapse begins. When one more column succumbs, those remaining will be deemed to no longer withstand the loading above, and will fail with post-bucking resistance offered by the 41 unscathed columns, and act to slow down the motion of the block of storeys above. However, their post-buckling resistance will be shown to be insufficient in preventing crush-down onto the floor below.

Fig. 2 shows a profile view of such a structure depicting four scenarios in one sketch. Scenario 1 is indicative of fires in storeys 41 and 40 while the rest of the building is free from fires of any kind. Scenario 2, illustrates a case where the fires are only occurring in storeys 31 and 30, etc. to Scenario 4, in which fires exist only in storeys 11 and 10.

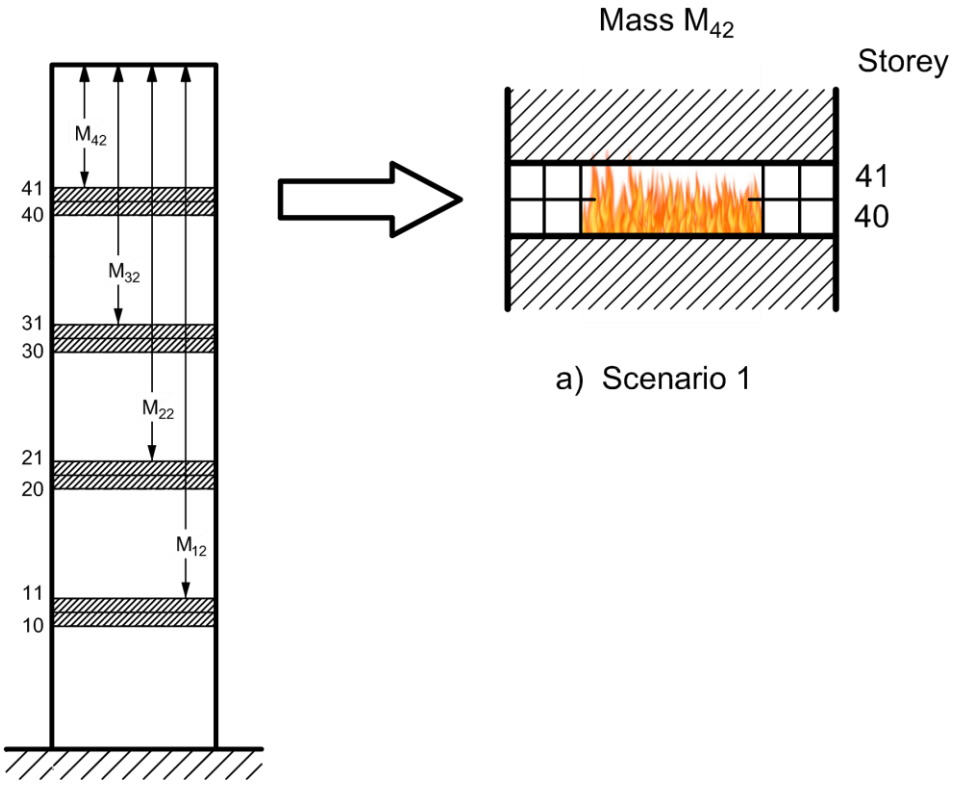

Fig. 2. Scenarios from 1 to 4 (raging fires on each of 2 storeys).

4. Dissipative Elements Resisting Collapse

In considering the columns which are deemed to be the major contributors to resisting storey-to-storey gravity loads, we assume therefore that 41 columns within a given storey are totally capable of providing post-buckling resistance to axial loads as opposed to the other 39 which are assumed to have been completely compromised by the fires raging in the storeys noted (i.e. 41 and 40 as noted in Fig. 2(a) for Scenario 1). An issue to be resolved is what value of axial resistance is appropriate when a column fails, but retains post buckling strength resistance. Bazant and Zhou (2002) chose to employ only bending resistance together with rotation capacity as being the measure of such energy absorption. As noted in an earlier paper (Korol and Sivakumaran, 2014), the vast majority of columns such as those employed in office buildings offer much greater energy dissipative values under axial loads than values computed employing standard plastic hinges under lateral loads only. Based on a set of experiments undertaken at McMaster University, axial energy dissipation in the

post-bucking range needs to be included. We do so indirectly by employing a factor defined as α, which is used to multiply the Plastic Bending energy part alone to account for both types of resistance. Indeed, our experiments on the equivalent of pin-end-ended columns showed values of α to be about 3.5 times the value obtained when that same member is subjected to a lateral load causing minor axis plastic bending alone.

We assume for storeys experiencing raging fires that the concrete in their floor areas offer no resistance through pulverization because of having experienced intense heat. However, other floors that have not been exposed to the fires are presumed to be resistant to break-up during the assorted impacts that will occur as storeys crush down onto lower levels. In this regard, our earlier work on the energy required to pulverize concrete slabs that contains shrinkage steel suggest that penetration loadings from beams and girders crashing onto them, will be resisted in accordance with the degree of pulverization, i.e. the extent to which floors are broken up into both very small and large sized particles through penetration loadings. An earlier paper (Sivakumaran et al., 2014) reported on our experimental findings involving concrete slabs with shrinkage reinforcement only, and arrived at an estimate of 4900 J/kg as an average value for the break-up under penetration loadings. We will use this figure for normal strength concrete having a density of 2400 kg/m^3, together with an average depth of floor slab of 101.4 mm (4”).

5. Fire Condition Scenarios

5.1. Scenario 1

Being very conservative in estimating resistances offered in storeys experiencing raging fires, we ignore any dissipative energy the presumed concrete floors would normally offer. Consequently, the only resistance assumed to contribute towards energy dissipation by steel members will involve 41 columns i.e. these being *almost* sufficient to support the loading above the storeys that are on fire, and noted as mass M_{42} in Fig. 2 for Scenario 1. Since the initial energy state has zero velocity the following equation therefore applies to this case:

$$½(M_{42})\,(v_{41}^{f})^2 = M_{42}\; g\; h - 41 \cdot 0.9\pi\, Z_y\, F_y^*\, \alpha\,, \qquad (1)$$

in which v_{41}^{f} is the final velocity of the upper block at impact with the 41st floor and Z_y is the plastic section modulus for bending about the section’s minor axis (CISC handbook, 2016). Note that we have assumed that plastic hinges form only at the mid-height of storeys, and do *not* form at floor levels, again under-estimating column absorptive energy capacity in the interest of being conservative. The 0.9π factor is an estimate of the angle rotated at mid- height as a given column is crushed, before encountering a floor’s crushed debris. Inserting the values noted in row 1 of Table 1, together with h = 4m gives the result of v_{41}^{f} = 7.71 m/sec.

Table 1. Column and total mass data for pertinent storeys.

Storey i	W-Shape	Z_y (mm^3)	F_y^* (MPa)	$\sum i^{51}(m_i + m_{cols}) \cdot 10^3$ kg $= M_{i+1}$
41	W360 x 162	1520	299.9	19483
40	“	“	“	21553
39	W360 x 179	1680	302.2	23529
38	“	“	“	25505
37	“	“	“	27480
31	W360 x 262	2680	305.2	39072
30	W360 x 287	2960	306.2	41082
29	“	“	“	43091
28	“	“	“	45096
27	W360 x 314	3240	306.3	47120
21	W360 x 382	4030	308.0	58750
20	“	“	“	60790
19	“	“	“	62790
18	W360 x 421	4490	310.4	64883
17	“	“	“	66936
16	“	“	“	68985
15	W369 x 463	4980	310.8	70989
11	W360 x 509	5550	311.6	78742
10	“	“	“	80823
9	W360 x 551	6050	312.0	82918
8	“	“	“	85072
7	“	“	“	87106
6	W360 x 592	6570	312.2	89214
5	“	“	“	91321
4	“	“	“	93428

Continuing with the analysis in the 40th storey, we employ the conservation of momentum principle to ascertain the initial velocity of the block crushing down into the 40th storey and which gives a value of v_{40}^{i} equal to 10/11 times 7.71 to give the initial velocity of 7.01 m/sec. in the 40th storey. The equation of motion then becomes:

$$½(M_{41})\left(v_{40}^{f}\right)^{2} = ½(M_{41})\,(7.01)^{2} + (M_{41})\,g\,h - 41\cdot 0.9\pi\,Z_y\,F_y^{*}\,\alpha\,. \quad (2)$$

Employing the values noted in the second row of Table 1 results in a value of v_{40}^{f} of 10.51 m/sec, followed by a reduced value of v_{39}^{i} of 9.63 m/sec. We are now dealing with a storey that has not experienced fires during this scenario and hence we need to account for all 80 columns and, if they are insufficient to stop the motion, pulverization of the 39th floor comes into play. The governing equations for such a case is:

$$(v_{39}^{f})^{2} = (v_{39}^{i})^{2} + 2gh - \frac{2\left[80\cdot 0.9\pi\,Z_y\,F_y^{*}\,\alpha - X\,(4.674\cdot 10^{9})\right]}{M_{40}}. \quad (3)$$

The numerator of the last term in Eq. (3) is the energy absorbed by concrete floor pulverization. Total floor destruction is indicated by $X = 1$, in which case the final velocity within that storey > 0 with motion continuing into the storey below, whereas a negative value of v^{f} would indicate that the motion stops with only part of the floor area energy dissipation needed by that floor's breakup. In our case, setting $v_{39}^{f} = 0$, and solving for X results in a value of 0.34 means that 34% of that floor is pulverized. We conclude, therefore, that the motion stops at the 39th floor. This result is given in the first row of Table 2.

5.2. Scenarios 2, 3 and 4

Similar calculations were performed for the other three scenarios that involved 2 storey fires. The pertinent data for Scenario 2 involved storeys 31, 30 and 29 in Table 1, while row 2 of Table 2 noted that motion stopped at the floor of storey 29, this time with 70% of the floor broken up. In the case of Scenario 3, it will be noted in Table 2 that crush-down extended an extra storey to level 18, with 38% pulverization, while Scenario 4 resulted in the most severe damage state with 4 storeys crushed and 77% of floor 8 suffering breakup. It is evident therefore that raging fires occurring at low rather than high levels in a building will result in a partial collapse that involves the greatest amount of damage to the structure.

5.3. Scenario 5

It is of interest to determine the extent to which a greater degree of structural damage occurs when 4 storeys are engulfed in fires. Such might be the case for circumstances when a building is struck by a jumbo-jet aircraft, for example, as we witnessed in New York City some years ago. In this particular scenario, fires are presumed to rage in storeys 41, 40, 39 and 38, and is shown in Fig. 3. For this Scenario, we will have equations similar to those noted for Scenario 1, but which require us to employ the data and do calculations for two additional levels involving stories 38 and 37. Employing Newton's laws of conservation of energy and the linear momentum principle as before, and with data obtained from Table 1, we determine that crush-down will destroy 5 storeys and result in 64% of the floor in storey 37 having been compromised before the motion stops. This means that about twice as much of the floor below the fire is subject to breakup as compared with Scenario 1 that involved two storey fires.

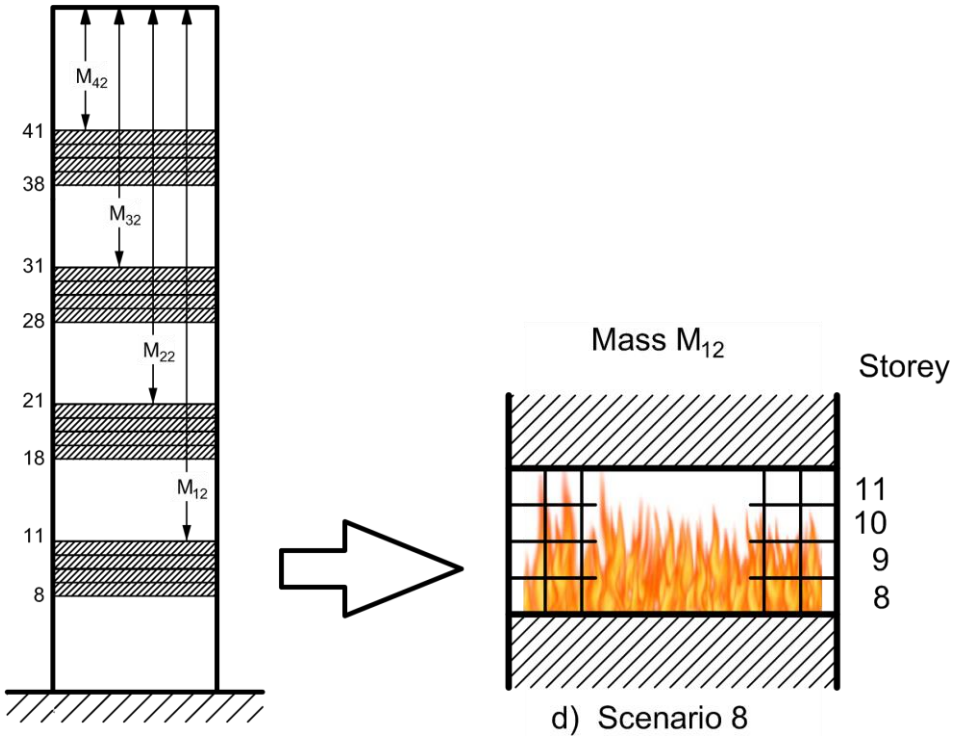

Fig. 3. Scenarios from 5 to 8 (raging fires on each of 4 storeys).

Table 2. Results of storey fires and computed states of collapse (based on steel yield stress = 345 MPa and S.F. = 2).

Scenario	Fires in storeys	Storeys crushed	Motion stopped in floor	Pulverization when motion stops
1	41,40	41, 40, 39	39	34%
2	31,30	31, 30, 29	29	70%
3	21,20	21,20,19, 18	18	38%
4	11,10	11, 10, 9, 8	8	77%
5	41, 40, 39, 38	41, 40 39, 38, 37	37	64%
6	31, 30, 29, 28	31, 30, 29, 28, 27, 26	26	46%
7	21, 20, 19, 18	21, 20, 19, 18, 17, 16, 15	15	49%
8	11, 10, 9, 8	11, 10, 9, 8, 7, 6, 5,4	4	63%

5.4. Scenarios 6, 7 and 8

These last three scenarios involve 4 storey fires at progressively lower levels akin to scenarios 2, 3 and 4. As observed from the last three rows of Table 2, an additional one or two storeys crush down occurs when compared to their scenario counterparts, 2, 3 and 4. Fig. 3 shows the storeys that are pertinent, i.e. 31, 30, 29 and 28 for Scenario 6, and so on, with our highlighting the last one as "d) Scenario 8". It represents the worst case in terms of damage to the structure since there are four additional storeys, 7, 6, 5 and 4 that crush down with the latter floor's area being pulverized by 63% before the motion stops.

6. Conclusions

As we noted in the Introduction, even the authors of the FEMA report pertaining to the collapse of the twin towers, purportedly due to fires primarily, did not advance a need for major changes to the applicable building codes at that time (FEMA, 2002). However, others, such as Bazant and Zhou (2002), Bazant and Le (2011) and NIST (2005, 2011) indicate otherwise. Our objective in this article has been to employ the present day building code that is applicable to high rise buildings and arrive at column sizes that meet the requirements of the CSA Standard (CAN/CSA S16-14) for non-core areas. These areas are less robust than are core areas, and hence represent a greater potential risk of collapse due to gravity driven loadings when extreme fire loads are present than would the overall structure experience.

Our focus has been to utilize principles that are easily understood, i.e. Newton's laws and employ assumptions commensurate with energy absorption elements that include plastic hinge buckling at mid height storeys that are subject to progressive collapse, and to concrete floor slabs that will breakup when struck by falling steel floor beams and girders. In the interest of being conservative, we have excluded any twisting and bending of these floor support members, the fasteners that yield and/or fracture, the arrays of non-structural partitions, desks, bookcases, filing cabinets etc. that are present in occupied office spaces.

Despite our neglecting so many such crush resisting components, we found that for cases where fires raged on two adjacent floors (4 scenarios including top, bottom and intermediate cases) that the one giving rise to a maximum amount of structural damage was Scenario 4. Fires in storeys 10 and 11 resulted in collapse of 2 storeys below, i.e. 9 and 8. For storey 8, the motion of the upper block stopped when 77% of a floor broke up.

When four adjacent floors experience extremely hot fires, crush-down failures do cause more than two storeys below to fail. In the case of Scenario 8 that involved fires on floors 8 to 11 inclusive, storeys 7 down to 4 suffered collapse, with the motion stopping with 63% of the 4th floor subject to breakup.

Since complete collapse in crush-down for even the most severe case of fires on four adjacent floors conceived in our study did not happen, we have to conclude that fire events of any reasonable description will not cause a steel framed building to collapse – partial collapse of some storeys? Yes, unfortunately, but overall collapse? No.

In that regard, code writers might wish to caution owners of high rise buildings that occupants ought to be warned about the possibility, slight as it might be, of some floors immediately below those experiencing *raging* fires to collapse, but not to panic. Storeys distant from those so engulfed would likely provide a temporary safe haven. Of course, smoke inhalation is another issue that such standards might need to embrace. Clearly, other means of protection which were beyond our study such as proper exits, sprinkler systems, alarms etc. are vitally important in saving lives.

Appendix A. Design Parameters Associated with Scenario 1

The following subsections provide the basis for the design of the columns in storeys 40 and 41.

a) For design purposes we must select what are known as specified values for L and D which for office buildings the values prescribed are taken as 2.4 kPa and 3.6 kPa respectively for floors. Employing load factors of 1.5 for L and 1.25 for D that include roof loadings assumed to be equivalent to that for a typical floor, and, estimating the

self weight of columns above the 40th (10 levels), we get a factored load of 80 [8.1 x 49 x 11 x 10^3 + 105 x 4 x 10 x 9.81] = 353 x 10^6 N. Meanwhile the factored resistance for a single column of size W360x162 is computed to be 5560 kN for an unsupported length of 4m, the computation of which is given in Appendix 2. It follows, then, that for 80 columns prior to the fires the factored resistance is 5560 x 80 x 10^3 = 444.8 x 10^6 N, or about 26% higher than the factored load. (Had we selected a lighter section, it would have required filler plates to accommodate depth dimension discrepancy with the 360W179 section selected immediately below). The top two rows of Table 1 indicate the W-shape selected and the Z_y and F_y^* associated with the storeys that relate to the fire events pertaining to Scenario 1.

b) The computation of mass M_1 (block above storey 41) arising from *expected* live and dead loads during a fire, or in general, normal occupancy, involves prescribing a value lower than that proposed for the design. As such, we select 0.5 L, for the former, with dead loading equal to that specified, i.e. D in storeys 42 to the roof inclusive, i.e a total of 10 levels. We then calculate a value of load applied that when converted to mass units, works out to be 19,180 x 10^3 kg. Accounting for the self weight of the columns for 9 levels, gives an adjusted total tally of 19,483 x 10^3 kg (i.e. an average of 105 kg/m) and noted in the top row of Table 1. The 40th storey will, of course be subject to an additional level of loading for which the tally becomes 21,553 x 10^3 kg, noted in the second row. As pointed out previously, an adequate factor of safety (of about 2), results in our selecting an H-shape designated as 360W162 for these two levels, with a computed resistance in mass units of (5560 x 80 x 10^3)/9.81 = 45,340 x 10^3 kg, a value which is 2.1 times that of the expected applied loading. This size is reasonable for gravity forces only, since the core areas are deemed to provide much of the lateral resistance to withstand anticipated maximum wind or earthquake loads. However, it should be noted that expansion of structural members due to temperature effects which can result in additional stresses due to restraining forces from floor systems will have unspecified consequences in reducing the factor of safety to a minor extent, perhaps lowering it to just under 2.

Appendix B. Factored Resistance of Columns (Storey 40 & 41)

While F_y is presumed to be 345 MPa, a reduction factor is required to account a column's effective length and radius of gyration values. The formula that is applicable by the Canadian code is based on the parameter $\lambda = KL/r\,(F_y/\pi^2E)^{1/2}$ in which KL = 4000 mm, $r_{\min} = r_y$ = 95 mm, and E = 200,000 MPa. For a W360x162 section, λ = 0.557. The empirical factor, which the code adopted is computed as $[1+0.557^{2.68}]^{-0.7463}$ = 0.8685, that when multiplied by F_y gives the value of F_y^*, or 299.6 MPa, as noted in Table 1.

References

Bazant Z, Le J-L (2011). Why the observed motion history is smooth. *Journal of Engineering Mechanics, ASCE*, 137(1), 82-84.

Bazant Z, Zhou Y (2002). Why did the World Trade Center collapse? - Simple analysis. *Journal of Engineering Mechanics, ASCE*, 128(1): 2-6, Addendum, 128(3), 369-370.

CISC (2016). Handbook of Steel Construction. 11th Edition, Part 6 - Properties and Dimensions, Canadian Institute of Steel Construction, Markham, Ontario.

CSA (2014). Design of steel structures. CSA Standard CAN/CSA S16 – 14, Canadian Standards Association, Rexdale, Ontario, Canada.

FEMA 403 Report (2002). World Trade Centre building performance study: data collection, preliminary observations and recommendations.

Hall JR Jr. (2014). The total cost of fire in the United States - a report for the National Fire Protection Association - fact sheets, 3 pages.

Korol RM, Greening F, Heerema P (2015). Performance-based fire protection of office buildings: A case study based on the collapse of WTC 7. C*hallenge Journal of Structural Mechanics*, 1(3), 96-105.

Korol RM, Sivakumaran KS (2014). Reassessing the plastic hinge model for energy dissipation of axially loaded columns. *Journal of Structures*, ID 795257, 7 pages.

McAllister TP, Sadek F, Gross JL, Kirkpatrick SW, MacNeill RS, Bocchieri R, Zarghamee MS, Erbay OO, Sarawit AT (2013). Structural analysis of impact damage to World Trade Center buildings 1, 2 and 7. Fire Technology, 49(3), 615-642.

NIST (2008). Final report on the collapse of World Trade Center Building 7. National Institute of Standards.

NIST (2012). Questions and Answers about the NIST WTC 7 Investigation (June update). National Institute of Standards.

Quintierre JG, Williams FA (2014). Comments on the NIST Investigation of the World Trade Center fires. *Journal of Fire Sciences*, 32, 281-291.

Sivakumaran KS, Korol RM, Fan X (2014). Energy absorption potential of concrete floors containing secondary (shrinkage and temperature) reinforcements. *Frontiers of Structural and Civil Engineering*, 8(3), 282-291.

Wikipedia (2018). Factor of Safety. https://en.wikipedia.org/wiki/Factor of safety, Downloaded on 15-04-2018.

Challenge Journal of Structural Mechanics

Research Article

Optimum design of purlin systems used in steel roofs

İbrahim Aydoğdu [a], Mukaddes Merve Kubar [a], Dahi Şen [a], Osman Tunca [b,*], Serdar Çarbaş [b]

[a] *Department of Civil Engineering, Akdeniz University, 07058 Antalya, Turkey*
[b] *Department of Civil Engineering, Karamanoğlu Mehmetbey University, 70100 Karaman, Turkey*

ABSTRACT

In this study, one existing purlin system which is used in steel roof is optimized by taking into account less cost and bearing maximum load via developed software. This software runs with firefly algorithm which is one of the recent stochastic search techniques. One of the metaheuristic techniques, so-called firefly algorithm imitates behaviors of natural phenomena. Behaviors and communications of firefly are inspired by this algorithm. In optimization algorithm, steel sections, distance between purlins, tensional diagonal braces are determined as design variables. Design loads are taken into account by considering TS498-1997 (Turkish Code) in point of place where structure will be built, outside factors and used materials. Profile list in TS910 is used in selection stage of cross sections of profile. Constraints of optimization are identified in accordance with bending stress, deformation and shear stress in TS648. Design variables of optimization are selected as discrete variables so as to obtain applicable results. Developed software is tested on existing real sample so; it is evaluated with regard to design and performance of algorithm.

ARTICLE INFO

Article history:
Received 11 December 2017
Revised 20 March 2018
Accepted 25 May 2018

Keywords:
Structural optimization
Purlin system in steel roofs
Firefly algorithm
Stochastic search technics

1. Introduction

Approach of civil engineers to engineering problems inclines safety, economy and aesthetic. Among these, if anyone is ignored, solution of engineering problem will be insufficient. Therefore, it is not enough that a developed system has required functional conditions (Esen and Ülker, 2008). So, all systems which will be designed must require to be economic beside providing required functional conditions. Yet, it is quite difficult to do via traditional designs and solution methods when discussed engineering problems have complex structure which includes nonlinear material properties, multiple variables and est. properties. To analyze these complex problems, there are various software which include optimization tool. Çiftçioğlu et al. (2017) is investigated wind load design for hangar with different geometry via finite element method. Akpınar et al. (2017) optimize transportation system by using simulation software. Using optimization methods has been widespread for these problems. As a structural optimization example, Değertekin et al. (2007, 2008) optimize linear and nonlinear geometric steel frame systems by accepting minimum cost as objective function. Optimization is a method that can find suitable solutions in line with target or targets under specific conditions (Keleşoğlu and Ülker, 2005). Optimization is investigated in three main categories as topology optimization, shape optimization and size optimization according to the problem. (Erdal et al., 2011; Mooneghi and Kargarmoakhar, 2006; Rong et al., 2000). In the same way, optimization is investigated according to solution methods as deterministic and stochastic methods. Metaheuristic optimization techniques which are designed by inspiring natural phenomena are developed under randomness optimization methods. These methods become popular with based on probability effective solutions without need complex mathematical equations (Yang et al., 2003).

There are various metaheuristic search techniques available in the literature for structural optimization problems. Genetic algorithm, evolutionary algorithm, ant colony algorithm, particle swarm optimization and artificial bee colony algorithm etc. can be indicated as samples (Sonmez et al., 2013). In this study, an optimum

* *Corresponding author*. Tel.: +90-338-2262000 ; Fax: +90-338-2262214 ; E-mail address: osmantunca@kmu.edu.tr (O. Tunca)
ISSN: 2149-8024 / DOI: https://doi.org/10.20528/cjsmec.2018.03.002

design software is developed by using among them firefly algorithm that is one of the randomness optimization techniques. Sizes of purlin systems frequently used in steel roof structure are optimized to can carry snow load, earthquake load, wind load, dead load and to have minimum weight. Loading condition in problem, strength constrains and geometric constrains are considered from Turkish Standards (TS). In order to obtain applicable results, discrete variables are used in optimum design algorithm. In this way, option of steel profile used in solution is selected from profile table in TS910. Obtained results by using optimum design software which based on firefly algorithm are investigated with regarding to both of design and performance of algorithm.

2. Purlin Optimization Method

Purlins are one of the basic member of roof structure. Acting on the load to the structure such as live load, dead load and wind load is transmitted to other structural member by means of purlins. Additionally, they support to roof deck. These structural members are used commonly. Optimization of structural member which so often used in building sector is quite important in cost. Conception of optimization is essentially investigated in two main options as scholastic and deterministic. In stochastic method which is used in this study, randomness is utilized in the process of optimization. Firefly algorithm which is one of the stochastic optimization techniques is a metaheuristic method which is designed by inspiring natural phenomena. Firefly algorithm is developed by observing social behaviors of firefly which live in tropical regions and by imitating these behaviors.

2.1. Firefly algorithm

The name of firefly algorithm, it is developed by Yang et al. (2009), come from firefly which live in tropical region and which is taken sample when selection stage of algorithm. Chemical is identified as ''lusiferine'' is used in organ which products light. ''lusiferine'' react with Oxygen and ''lusiferase'', that is name of other chemical. In this way, light is produced. Attraction of a firefly is directly proportional to its shine. There are several similarities about this algorithm and other metaheuristic based optimization methods. But, it is generally easier in applications. According to researchers, main purpose of producing light is to attract attention of other fireflies by sending signal. Among estimated other purpose, there are to find friends, to take potential prey and to protect itself from hunter. Genders of fireflies are not considered. Therefore, it is assumed that all of the fireflies have same gender. Because of there is not gender gap, the more fireflies are shiny, the more they have attractiveness. Distance between fireflies decreases light of fireflies. Thus, attraction between fireflies decreases. If a firefly sees brighter than itself, it moves to this seen. If most shiny firefly is itself, firefly will move randomly. In algorithm, each firefly is represented by a design variable. Objective function value is represented by light of fireflies. Design vector (value of design variable) is linked to position of fireflies. It is possible to summarize steps of firefly optimization algorithm as below (Değertekin et al., 2015);

<u>*First step: Initializing of parameter and generating positions of firefly:*</u> Firstly, parameters of optimization are defined such as number of firefly (n), randomness coefficient (α), brilliancy (β_0) and distance (γ). After the parameters of algorithm are defined, starting positions is randomly selected according to following equation.

$$\boldsymbol{x}_{i,j}^{0} = \boldsymbol{x}_{j,min} + rnd \cdot \left(\boldsymbol{x}_{j,max} - \boldsymbol{x}_{j,min}\right) \; .$$
$$i = 1,2,\dots,n \;\; ; \;\; j = 1,2,\dots,td \tag{1}$$

In the above equation, *rnd* is a random value generated between 0 and 1, $\boldsymbol{x}^{0}_{i,j}$ is defined as value at number *i* firefly in the moment of initializing (t=0) and at number *j* dimensions, $\boldsymbol{x}_{j,max}$ is maximum limit of number *j* design value, $\boldsymbol{x}_{j,min}$ is limit of number j design value and *td* is total number of the design variables (dimension number of problem space). Performance of fire fly is investigated at current positions, after beginning position generate. In other words, values of objective functions ($f(\boldsymbol{x})$) are calculated by using assigned designs to firefly. After this process, designs and value of objective functions which is calculated by using design values are saved to algorithm memory.

<u>*Second step: Determination of light intensity of fireflies:*</u> In this step, light intensity of fireflies ($\boldsymbol{I}$) is determined as related to objective functions value of assigned design. In this study, cost minimization is purposed. Cost of purlin system which is used in steel roof is inversely proportional to their weight. So, light intensity is determined according to below equation.

$$\boldsymbol{I} = \frac{1}{f(\boldsymbol{x})} . \tag{2}$$

<u>*Third step: Updating position of fireflies:*</u> In this step, fireflies move to others which have more attractiveness. Modification of positions is updating design in firefly algorithm. Modification of position equation which is developed by depending on Levy flight theorem is formulized below.

$$\boldsymbol{x}_{i,j}^{t+1} = \boldsymbol{x}_{i,j}^{t} + \beta_0 \cdot e^{-\gamma r_{i,k}^{2}}\left(\boldsymbol{x}_{i,j}^{t} - \boldsymbol{x}_{k,j}^{t}\right) + \alpha \cdot \varepsilon_i^{t} \; .$$
$$i,k = 1,2,\dots,n \;\; ; \;\; j = 1,2,\dots,td \tag{3}$$

In Eq. (3), t is number of steps, k index show fireflies which is determined to approach by number *i* firefly, ε is a weight coefficient which explains of new position of fireflies and $r_{i,k}$ distance between fireflies number *i* and number *j* respectively. Euclidean distance $r_{i,k}$ is calculated by Eq. (4).

$$r_{i,k} = \sqrt{\sum_{j=1}^{td}\left(x_{i,j} - x_{k,j}\right)^2} , \tag{4}$$

<u>*Fourth step: Revaluation of fireflies by considering updated positions:*</u> Objective function values of design of

fireflies which updated positions in previous stage are calculated similarly with end stage of first step and memory of algorithm is updated. Best firefly in the memory is saved and it is returned to second step. Processes between second and forth steps iterates until it reaches maximum number of cycle. Best solution in memory of algorithm at the end of iterative solutions is considered optimum result.

3. Mathematical Model of Purlin Optimization

In this study, software which has the capability of optimum design is developed. For this purpose, purlin design problem is converted to optimization problem and, mathematical model of problem is created. Generally, modeling of optimization problem consists of three main parts, objective function, design variables and design constrains. Objective function is identified as purpose which is converted to mathematical function. Main purpose in optimization problem of steel roof purlin systems is to minimize cost of purlin structure. Objective function can be identified for purlin systems design optimization as below.

$$M(\boldsymbol{x}) = M_k + M_a + M_p + M_g \,. \tag{5}$$

In objective function equation above, M is total cost of purlin in steel roof, M_k is total welding cost in production of purlin, M_a is total anchoring cost in production of purlin, M_p is total cost of profile which will be used and M_g is total cost of brace which will be used during construction phase.

Design variables are one of the three main parts of optimization which can change objective function value. In problem of purlin system optimization, distance between purlins, slope of roof, cross section of profile, type of roof covering are design variables which directly affect cost of purlin structure.

Obtained results from optimization problem must provide necessary certain conditions. Constrains of purlin system optimization problem are strength constrains, displacement constrains and geometric (application) constrains. Obtained design must provide conditions of TS (Turkish Standards) which is shown below. These are limiters of optimization problem. There are three main verifications of TS to investigate purlin system design. These are classified as strength verification, displacement verification and shear verification.

Strength behavior constrain:

$$\sigma_{max} = \frac{M_x}{W_x} + \frac{M_y}{W_y} \leq \sigma_{em} \,. \tag{6}$$

In Eq. (6), M_x and M_y are moment values which occur on the profile in x and y dimensions respectively. W_x and W_y are static moment value which can be changed regard to cross section of profile and are imported from table of considered standard.

Displacement behavior constraints:

$$f = \sqrt{f_x^2 + f_y^2} < \left(\frac{l_k}{300}\right) cm \,,$$

$$f_x = \frac{2.48 q_x l_k^4}{I_x} \quad , \quad f_y = \frac{2.48 q_x l_k^4}{I_y} \quad . \tag{7}$$

In Eq. (7), f_x and f_y are displacement of purlin in x and y dimensions, l_k is purlin span and I_x and I_y are moment of inertia in x and y axis respectively.

Shear behavior constrains:

$$T_x = q_y * \frac{L_0}{2},$$

$$\tau_x = \frac{T_x}{\frac{5}{3} * (F_{başlık})} \leq \tau_{em} \quad , \quad \tau_y = \frac{T_y}{F_g} \leq \tau_{em} \quad . \tag{8}$$

Used in Eq. (8), T_x is shear force on the purlin, τ_x and τ_y are shear stress which will occur on the purlin, F_b is cross section area of flans in compression, F_g is cross section area of web and q_y is value of distributed load.

4. Created Software for Design Optimization of Purlin Systems Used in Steel Roofs

A software is edited by using firefly algorithm which is mentioned above to be used optimum design of purlin systems in steel roofs. This software which splash screen is showed in Fig. 1, is edited at Windows environment by using Visual Basic programing language. Usage of software and visual properties is indicated below.

1. Windows which will be entered desired data is displayed to enter parameter of structure systems which will be optimized by running dimensions command that is "*Boyutlar*" in splash screen windows "*Ana Sayfa*" under the menu of optimize "*Optimize Et*". In this screen, there are entry box listed below;
   - Span of frame system (m)
   - Total length of structure (m)
   - Slop of roof (degree)
   - Type of roof covering
   - Steel grade
   - Snow region (by regarding to TS)
   - Altitude (m)
   - Elevation from ground (m)
   - Brace price per unit (TL/kg)
   - Profile price per unit (TL/kg)
   - Maximum load that 1m roof covering can carry (kg/m^2) (optionally)
   - Type of steel sections (IPN or IPE)

2. After that, windows which will be entered optimization parameters of firefly algorithm is displayed by clicking optimization parameters "*Optimizasyon Parametreleri*" under also optimize button "*Optimize Et*". (Figs. 2 and 3). This window provides to enter parameter of firefly algorithm which will be used for solution by user. Desired optimization algorithm parameters to run this software are listed below.
   - Number of fireflies
   - Randomness

- β coefficient
- γ coefficient
- Number of design variables
- Number of maximum cycle
- Tolerance

3. Location of text file which will be saved optimum results is selected to initialize optimization process by clicking main page command "*Ana Sayfa*" that is placed under the optimize menu "*Optimize Et*". Optimum design process is begun with start command "*Başla*". When optimization process is finished, the passing time for optimization, beginning and finishing times, average passing time for per iteration, number of iteration until optimum result is obtained and optimum design results can be seen in "*Optimum/Best Design*" box (Fig. 4).

Fig. 1. Splash screen of optimum purlin design software.

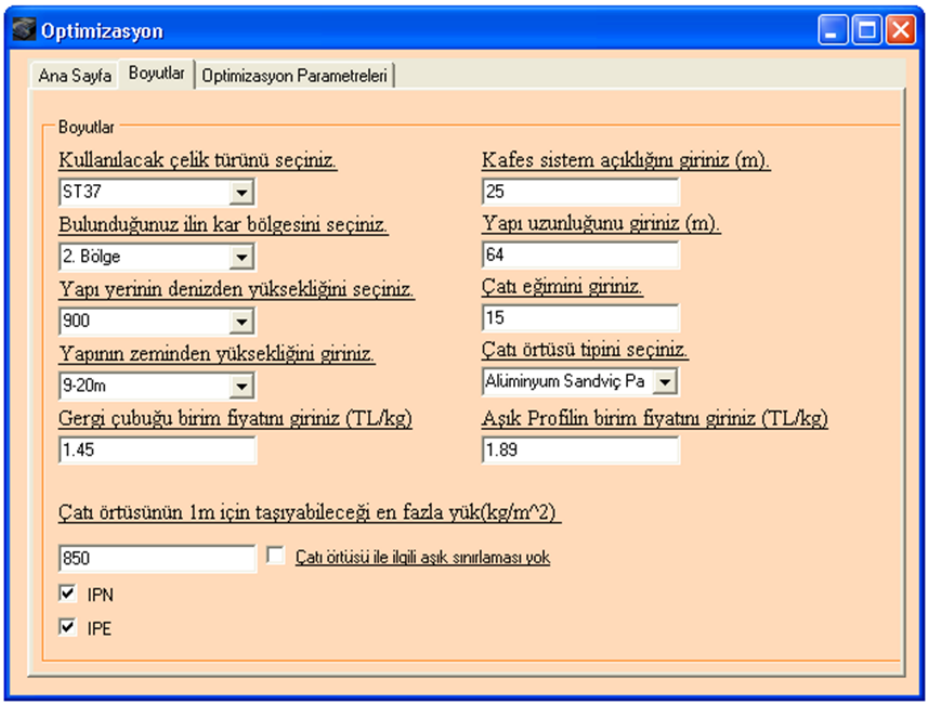

Fig. 2. Entries are requested from users by optimum purlin design software.

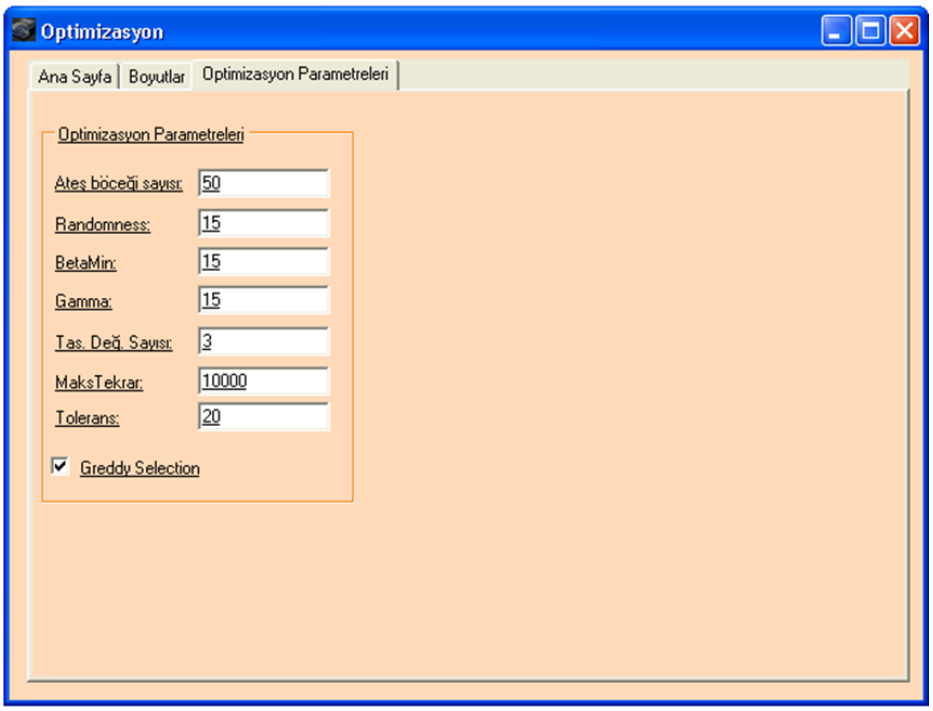

Fig. 3. Window, in which algorithm parameters of firefly method are entered.

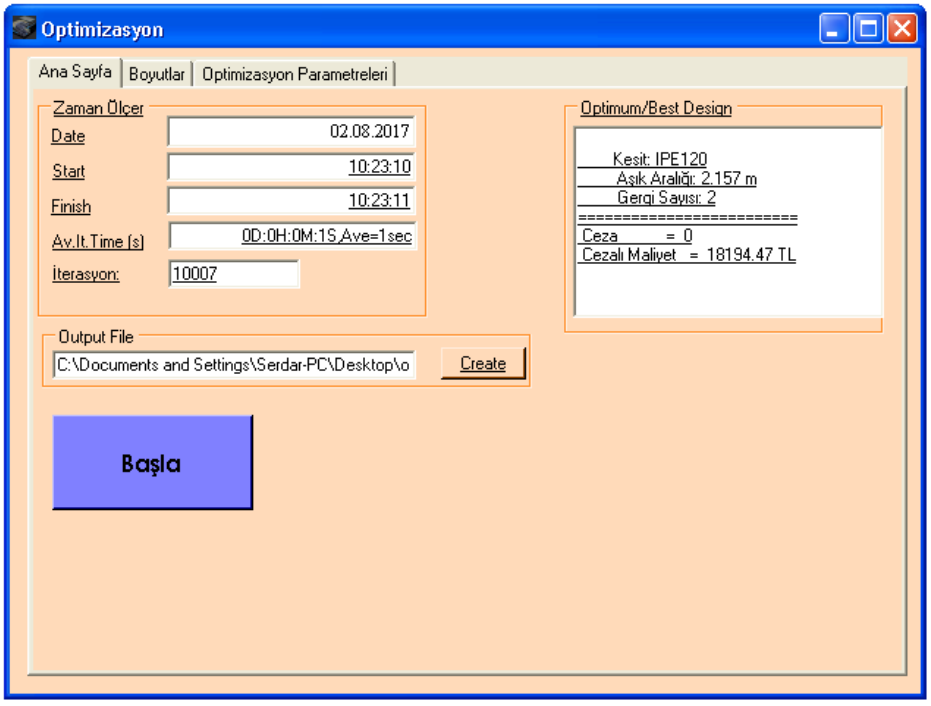

Fig. 4. Window, in which output of optimum results is displayed.

5. Design Sample

Developed software is tested on the sample which is recently projected. Detail of the project is shown in Table 1. Sample problem is calculated with optimization software. Obtained results from this solution are compared in cost of structure. This comparison is demonstrated in Table 2. When obtained result is investigated, developed optimization software obtains optimum purlin design which has about %32 less cost.

6. Conclusions

In this study, a software was developed to obtain optimum design of purlin systems of steel roofs by using firefly algorithm which inspires life style of fireflies. The main objective of this software is to minimize cost of steel purlin system in steel roof purlin system problem. Constraint functions of optimization problem were obtained by importing from verifications of TS-648 code. Results, which were obtained from optimization process,

must satisfy criterions of the Turkish Standards. Three different verifications were provided at the same time in order to design purlin systems which are used in steel roofs according to the Turkish Standards. These are axial stress verification, deformation verification and shear verification. Most important characteristic specifications of the software, which is used to design purlin system in steel roof, are ability of entry data and, ability to give result rapid and easily. Finding optimum solution of these structural systems, which is calculation of design, is quite complex and so easy owing to the structure of this software.

Table 1. Details of project.

Span of roof: 12 m	Height: 8 m
Length of roof: 51.6 m (10 span)	Slope of roof: 5°
Province: Kastamonu (3rd region)	Weight of roof covering: 50 N/m^2
Altitude: 800 m	Unit cost of steel (Brace/Profile): 1.9/2 TL/kg

Table 2. Comparison of purlin designs.

	Project Results	Optimum Results
Profile type of purlin	IPN140	IPE140
Distance between purlins (Horizontal Distance)	2m	3m
Type of brace (diameter of brace)	Single (ϕ8)	Double (ϕ8)
Max. Displacement / Limit	0.906cm / 1.72cm	1.384 / 1.72cm
Max. Stress / Limit	1011 / 1440 kgf/cm^2	1413 / 1440 kgf/cm^2
Cost of brace	158 TL	194 TL
Cost of profile	11806 TL	7997 TL
Total cost	11964 TL	8181 TL

Acknowledgements

This paper is based on a research project supported by the "2209-A University Student Scientific Research Projects Program- TÜBİTAK" with gratefully acknowledged.

References

Akpınar ME, Yıldızel SA, Karabulut Y, Doğan E (2017). Simulation optimization for transportation system: A real case application. *TEM Journal*, 6(1), 97-102.

Çiftçioğlu AÖ, Yıldızel SA, Yildirim MS, Doğan E (2017). Wind load design of hangar-type closed steel structures with different roof pitches using Abaqus CAE software. *TEM Journal*, 6(2), 336-341.

Değertekin SÖ, Hayalioğlu MS, Ülker M (2007). Tabu search based optimum design of geometrically non-linear steel space frames. *Structural Engineering and Mechanics*, 27(5), 575-588.

Değertekin SÖ, Hayalioğlu MS, Ülker M (2008). A hybrid tabu-simulated annealing heuristic algorithm for optimum design of steel frames. *Steel and Composite Structures*, 8(6), 475-490.

Değertekin SÖ, Lamberti L, Ülker M (2015). Uzay kafes yapıların ateşböceği algoritması yöntemiyle optimizasyonu. *XIX. National Mechanics Congress*, Trabzon, Turkey. (in Turkish)

Erdal F, Dogan E, Saka MP (2011). Optimum design of cellular beams using harmony search and particle swarm optimizers. *Journal of Constructional Steel Research*, 67, 237-247.

Esen Y, Ülker M (2008). Malzeme ve geometrik özellikler bakımdan lineer olmayan çok katlı çelik uzay çerçevelerin optimizasyonu. *Journal of the Faculty of Engineering and Architecture of Gazi University*, 23(2), 485-494. (in Turkish)

Keleşoğlu Ö, Ülker M (2005). Multi-objective fuzzy optimization of space trusses by Ms-Excel. *Advances in Engineering Software*, 36(8), 549-553.

Lukasik S, Zak S (2009). Firefly algorithm for continuous constrained optimization tasks. *Computational Collective Intelligence: Semantic Web, Social Networks and Multiagent Systems*, 5796, 97-106.

Mooneghi MA, Kargarmoakhar R (2016). Aerodynamic mitigation and shape optimization of buildings: Review. *Journal of Building Engineering*, 6, 225-235.

Rong JH, Xie YM, Yang X-Y, Liang QQ (2000). Topology optimization of structures under dynamic response constraints. *Journal of Sound and Vibration*, 234(2), 177-189.

Sonmez M, Sevim O, Kılıc M (2013). Topology optimization of double-curved double-layer grids. *2nd International Balkans Conference on Challenges of Civil Engineering, BCCCE*, Tirana, Albania, 1-8.

TS 498 (1997). Calculation Values for the Loads to be considered in the Design of Structural Elements. Turkish Standards Institute, Ankara.

TS 648 (1980). Building Code for Steel Structures. Turkish Standards Institute, Ankara.

TS 910 (2009). Hot Rolled -I- Beams. Turkish Standards Institute, Ankara.

Visual Basic Programing Language (2018). Microsoft Corporation Inc., Redmond, Washington, United States.

Yang XS (2009). Firefly algorithms for multimodal optimization, in stochastic algorithms: foundations and applications, *5th International Symposium, SAGA 2009*, Sapporo, Japan, 169-178.

Yang XS (2013). Multiobjective firefly algorithm for continuous optimization. *Engineering with Computers*. 29(2), 175–184.

Yang XS, Cui Z, Xiao R, Gandomi AH, Karamanoglu M (2013). Swarm Intelligence and Bio-Inspired Computation. Elsevier.

Challenge Journal of Structural Mechanics

Research Article

Finite element analysis of pre-stressed steel arch beams

Erkan Polat [a,*], Barlas Özden Çaglayan [b]

[a] *Department of Earthquake Engineering, İstanbul Technical University, 34457 Istanbul, Turkey*
[b] *Department of Civil Engineering, İstanbul Technical University, 34457 Istanbul, Turkey*

ABSTRACT

Techniques are being developed day-by-day to make it possible to pass through larger openings using smaller beam-column sections. Parallel to this trend, there is another necessity to produce not only smaller but also more economical and architecturally attractive beams. The aim of this study is to explain the structural behavior of steel arch beams reinforced using post-tension cables. Due to the effect of these, the arch beam load carrying capacity increases and a smaller sized optimized section can be obtained with a better architectural view. Moreover, it also allows better mechanical and applicable solutions for buildings. For a better understanding of the behavior of the reinforced beam, a steel beam and a steel arch beam with post-tensioned cables were modeled and analyzed using the SAP2000 finite element analysis computer program and compared with each other. In addition, full-scale specimens were prepared for testing to determine the structural behavior and compare the results with those from the computer modeling, the outcome of which was very promising. The similarity between the results inferred that no extra engineering knowledge and effort are needed to design such beams. The predicted (and proved by the testing) beam bearing capacity was 35% higher than that of the unreinforced beam. With just three full-scale tests completed, it was evident that the ratio (35%) could be increased by adjusting the cable post-tension force on much smaller sized beams.

ARTICLE INFO

Article history:
Received 5 December 2017
Revised 21 February 2018
Accepted 25 May 2018

Keywords:
Steel arch beams
Pre-stressed cables
Finite element analysis
Buckling analysis
Real model testing

1. Introduction

In the literature, research has been published to produce sophisticated design solutions for engineering problems and/or assemblies. Furthermore, the findings in this study also offer a sophisticated assembly strategy for long span beams that allows small beam sizes. At the same time, curbing building costs as well as allowing for architectural considerations in terms of aesthetic appearance are targeted in this study.

Using different materials or members is a method of improvement, and in this sense, the aim of this study was to use steel beams post-tensioned by cables in the same assembly. The cables, which can only carry tension forces, were placed at the tension zone of the beam. In order to increase the effect of the cable pre-tension force on the beam, the lower flange of the latter is shaped like an arch and a cable was connected to the beam-ends. The selected cable radius was 28 mm and nearly 10 t of pre-tension force was applied to it. Thus, with the reverse moment generated by post-tensioning of the cable in the beam, the bearing capacity was increased in the first step.

Beam sizes and spans can be very different depending on the requirement, thus a comparison was made between the actual test model of the beam and the finite element model, and the beam dimensions given in Fig. 1 were found to be within the scope of the testing possibilities.

In this study, increasing the arch of the beam bending and buckling load capacity with finite element buckling analyses and real laboratory test results were proven.

* *Corresponding author*. Tel.: +90-216-5507079 ; E-mail address: e.polat.m@gmail.com (E. Polat)
ISSN: 2149-8024 / DOI: https://doi.org/10.20528/cjsmec.2018.03.003

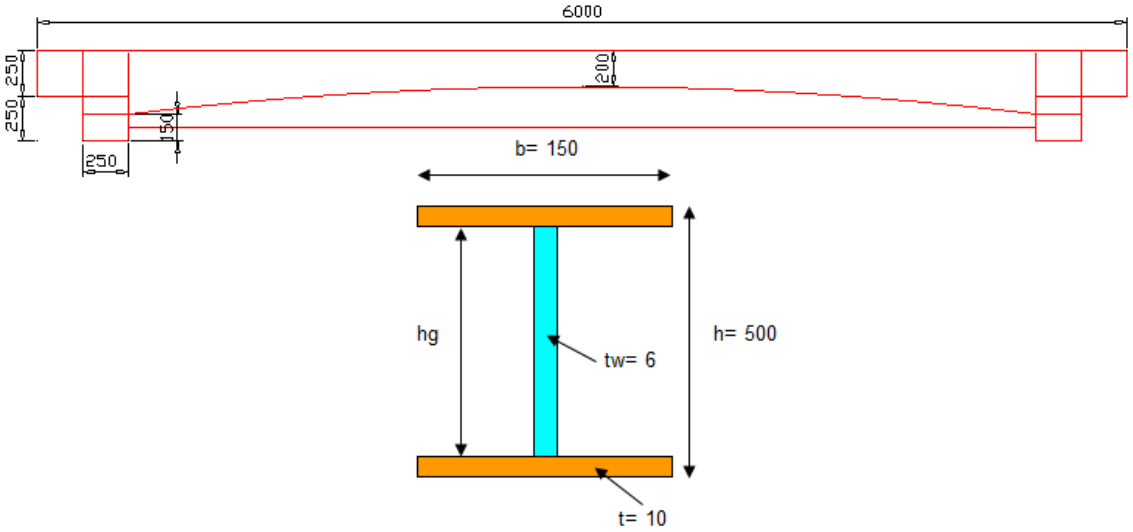

Fig. 1. Cross-section properties of the beam.

2. Section Properties

2.1. Materials

Steel beam flange and web plates : S235 JR
Cables : TS 1918 / 14 (AISI 316) (ϕ28 mm)
f_u = 180 kgf/mm²

2.2. Compactness

The section flange and web properties should provide compact section limits that prevent local buckling occurrences. Accordingly, the requirements for section properties were fulfilled by the section ratios selected, as can be seen in Eqs. (1a) and (1b) (AISC 360, 2010).

$$\frac{b}{2t} < \left(0.38\, x \sqrt{\frac{Es}{Fy}}\right) \quad , \quad 7.50 < 8.87 \surd \quad , \tag{1a}$$

$$\frac{hg}{tw} < \left(3.76\, x \sqrt{\frac{Es}{Fy}}\right) \quad , \quad 80 < 111.2 \surd \quad . \tag{1b}$$

2.3. Compression flange safety stress

Because of the variable section shape of the beam, compression safety stress changed along with section height. Maximum stress occurred at the mid-section of the span, thus the safety stress of the beam was calculated based on this location according to IMO - 02/2008 (2008) as follows:

$$\sigma_{B,\gamma} = \frac{2}{3}\left[1.0 - \frac{\sigma_a}{6B\sqrt{{\sigma_{s\gamma}}^2 + {\sigma_{w\gamma}}^2}}\right]\sigma_a \le 0.6\sigma_a \ , \tag{2a}$$

$$\sigma_{B,\gamma} = B\sqrt{{\sigma_{s\gamma}}^2 + {\sigma_{w\gamma}}^2} \ , \tag{2b}$$

$$\sigma_{B,\gamma} = \sigma_a/3 \ , \tag{2c}$$

$$\sigma_{Bs\gamma} = \frac{8440}{h_s l d_0/A_b} \ . \tag{2d}$$

l : 600 cm
d_o : 20 cm
b : 15 cm
d_i : 50 cm
t_f : 1 cm
t_w : 0.6 cm
γ : 1,5 < 8,043

$$h_s = 1.0 + 0.0230\gamma\sqrt{ld_o/A_0} \ , \tag{2e}$$

$$h_w = 1.0 + 0.00385\gamma\sqrt{l/i_{\gamma 0}} \ . \tag{2f}$$

A_{ko} : 40.8 cm²
A_{bo} : 58.8 cm²
r_{ky} : 3.31
r_{by} : 3.1
h_s : 1.59
h_w : 1.08
σ_s : 1.803 t/cm²
σw : 0.314 t/cm²

$$\sigma_s = \frac{8440}{h_s l d_0/A_b} \ , \tag{2g}$$

$$\sigma_{w\gamma} = \frac{120000}{(h_w l/i_{\gamma 0})^2} \ , \tag{2h}$$

$$B = 1.0 + 0.37\left[1.0 + \frac{M_1}{M_2}\right] + 0.50\gamma\left[1.0 + \frac{M_1}{M_2}\right] \ge 1.0 \ . \tag{2i}$$

M_1 : 0 t.cm
M_2 : 914 t.cm
x : 0.55
y : 2.2
B : 4.85 > 1
σ_b : 1.528 t/cm2 > 0.80 t/cm2
1.528 t/cm2 < 1.44 t/cm2
σ_b : 1.44 t/cm²

3. Finite Element Modeling

3.1. Loads

The loads applied to the beam were chosen so that the safety stress remained within its limits as given by the codes. It was assumed that loads were distributed uniformly and were applied on the top flange of the beam. This distributed load was calculated by considering a beam spacing of 1 m as follows:

Live Load	: 1300 kg/m^2
15 cm Concrete Slab	: 375 kg/m^2
10 cm Screed Concrete	: 240 kg/m^2
Cover	: 70 kg/m^2
Total Dead Load	: 685 kg/m^2

3.2. Design

The arch beam was modeled using the SAP2000 finite element analysis software package with shell members. A pre-tensioning steel cable was also attached to the beam-ends (see Fig. 2). The top flanges of the beam were not fixed along the span against lateral buckling.

4. Analysis Results

4.1. Shell stress and displacement

The tension force obtained on the upper flange of the beam was slightly greater than the limit tension force given in code (IMO - 02/2008, 2008), as can be seen in Figs. 3 and 4. The displacement/deflection occurred in a negative direction with a value of -12.6 mm.

Additionally, the cable tension force raised up from 10 to 18.6 t where the carrying capacity of the cable safety load was 50 t.

-12.65 mm displacement was obtained on the mid of the beam under the dead and live loads with pretension. L/300 = 6000/300 = 20 mm > 12.65 mm.

The analysis of the pre-tensioned arch beam tested in this study was compared to the results obtained from a conventional (hot-rolled) beam having a constant section height of 500 mm, as can be seen in Fig. 5. It was assumed that the span length under the same applied loads was the same. It can be observed that the proposed arch beam bearing capacity could be increased 1.45 times compared to the conventional beam design based on the allowable stress design (AISC 360, 2010).

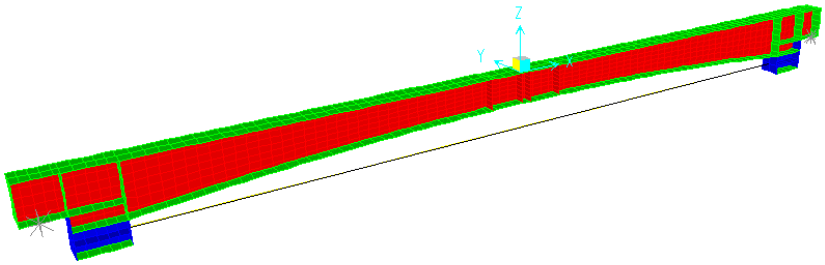

Fig. 2. Finite element model of the arch beam.

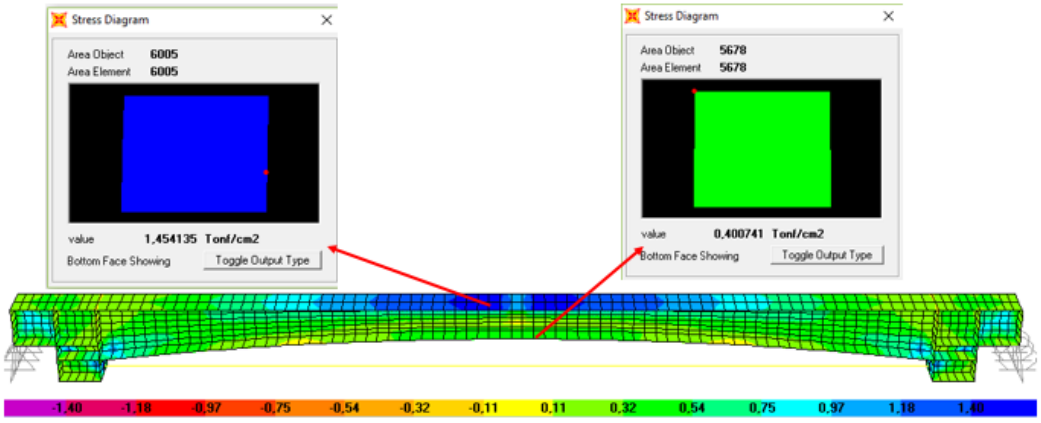

Fig. 3. Beam stress diagram (t/cm^2).

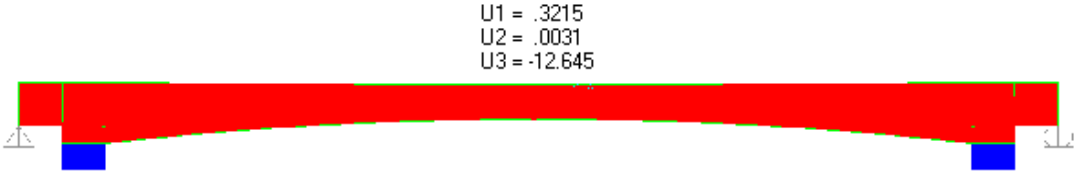

Fig. 4. Beam displacement dead + live load (mm).

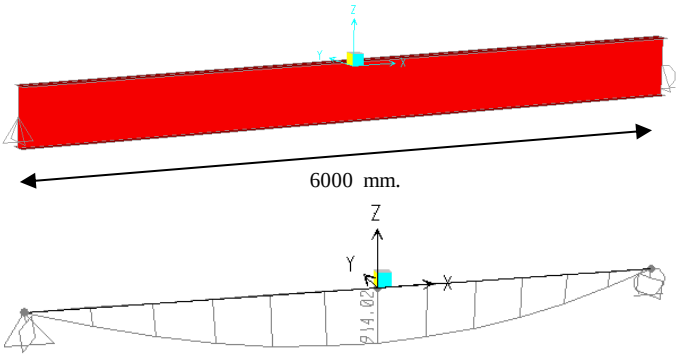

Fig. 5. Conventional I beam and moment diagram.

M 33 : 913.93 t.cm.
Mn / Ω : 629 t.cm (Beam moment capacity)

Beam capacity ratio : M33/(Mn/Ω) = 913/629 = 1.45 (AISC 360, 2010)

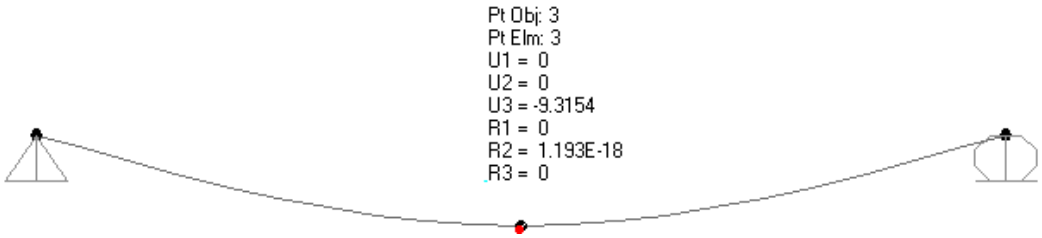

δ= 9.32 mm < 20 mm
Displacement values in directions; U1: X, U2: Y, U3: Z.

Fig. 6. Conventional I beam maximum vertical displacement.

The beam maximum vertical displacement (9.32 mm) was less than the arch beam displacement (20 mm), which is a disadvantage for arch beams under live loads, but the pre-tension is an advantage for dead and super dead loads because of the negative displacement.

4.2. Buckling analysis comparison

The conventional I beam and pre-tensioned arch beam buckling analysis results were compared with each other under the same given load.

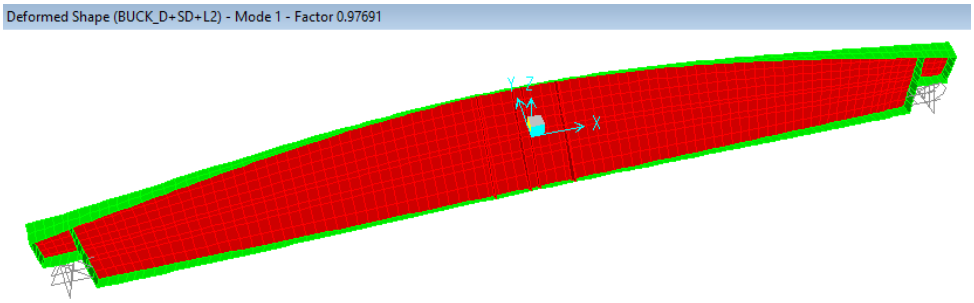

Fig. 7. Conventional I beam buckling analysis results.

Here, to obtain the same support conditions for a conventional beam modified as an arch beam, the conventional I beam first mode buckling factor was 0.977. This was not enough to be a safety concern since it is recommended that it is more than 2.

The first buckling factor of the arch beam was 2.765 in spite of the beam section size being reduced compared to the conventional I beam, which demonstrates a very important advantage of slender section beams. In this case, it was proved that the safety factor of the beam buckling was increased by the arch section and the pre-tension.

5. Specimen Tests

Three test specimens were produced according to the finite-element-analysis model-beam sizes and placed in the laboratory (see Fig. 9). The main loading frame consisted of HEA 300 profiles. These frames were analyzed under the maximum test load and capacity of the beam being tested.

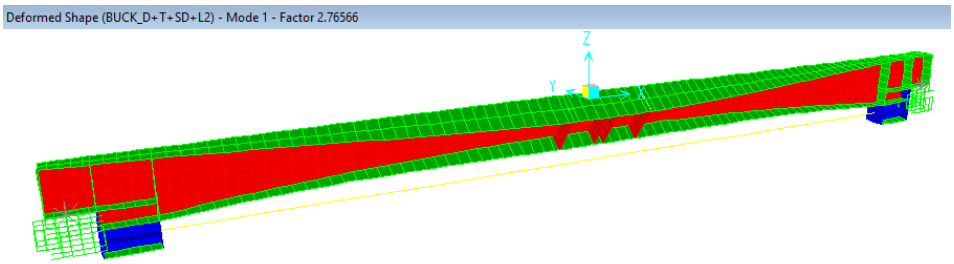

Fig. 8. Pre-stressed arch beam buckling analysis results.

Fig. 9. Test specimen.

One vertical and 3 horizontal displacement meters (linear variable differential transformers) were used. A total of 18 strain gauges were used on the test beam to measure the stresses and the tension in the rope. Two accelerometers were placed on the beams to monitor horizontal and vertical vibrations and another one was placed on the cable.

The first two samples were tested by increasing the applied loads up to the beam flange reach the yield limit. And second time, same two samples were forced to the ultimate state so that their bearing capacities were obtained, and the remaining one sample was loaded without a cable. Finally, total 5 tests were completed.

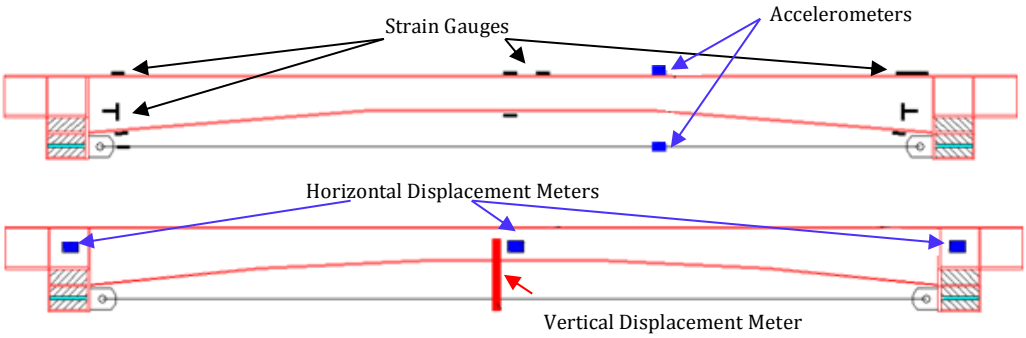

Fig. 10. Locations of the displacement meters, strain gauges, and accelerometers.

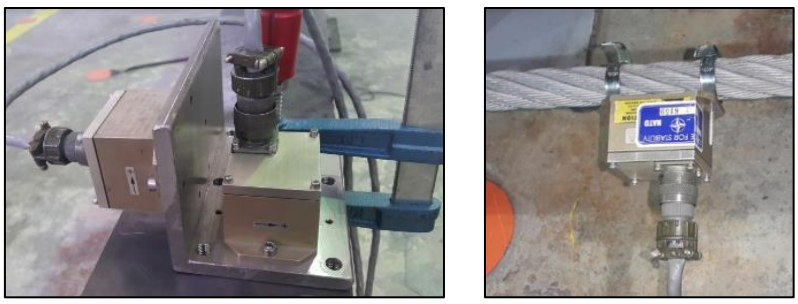

Horizontal & Vertical Accelerometer Cable Accelerometer

Fig. 11. Accelerometers.

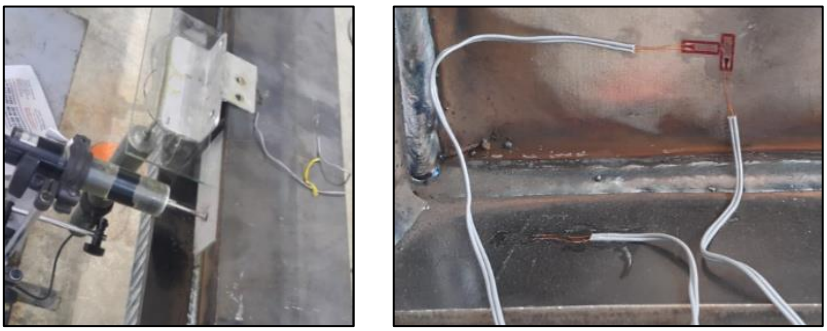

Fig. 12. Displacement transducers and strain gauges.

To measure the cable force, the results from the accelerometer and strain gauges were evaluated together. For this, the formulas reported by Wang et al. (2000):

$$T = 4ml^2 \frac{f_n^2}{n^2}, \tag{3}$$

and Humar (1990):

$$T = 4ml^2 \frac{f_n^2}{n^2} - \frac{EI}{\beta}(n\pi)^2, \tag{4}$$

were used and the values compared with the test results obtained from the strain gauges. However, according to the formulas, they were quite different from the strain gauge results.

Finally, the recordings of the accelerometers on the cable were transformed using the formulation developed by Fang and Wang (2012), and it can be seen that the results were subsequently very close.

In Fig. 13, the computer model and the results obtained from the test (test number 4) were demonstrated comparatively by applying a vertical concentrated load of 10 t. The test results were arranged in the Excel program and show the relevant parts of the beam image.

The strain distribution in the pre-tensioned arch bridge proposed in this study according to the test results recorded from the strain gauges is shown in Fig. 15.

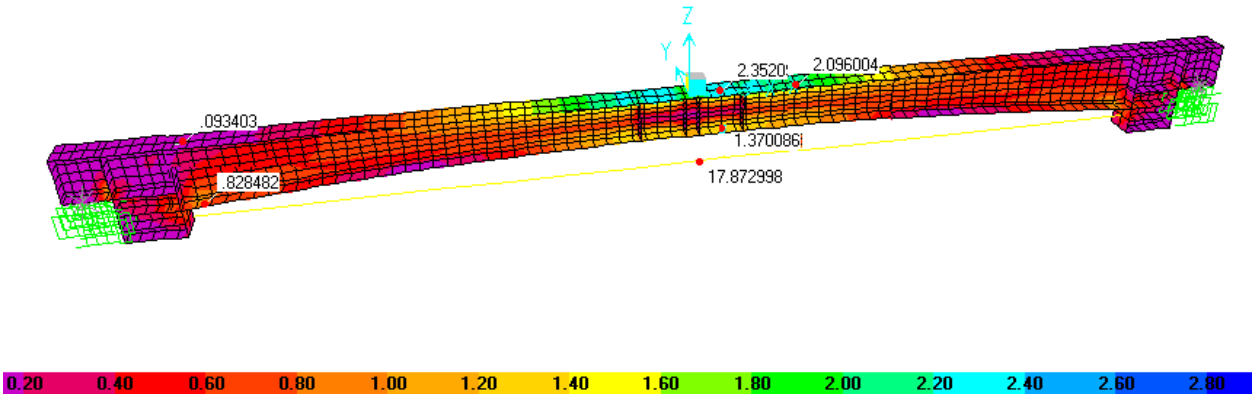

Fig. 13. Beam stress distribution (t/cm²).

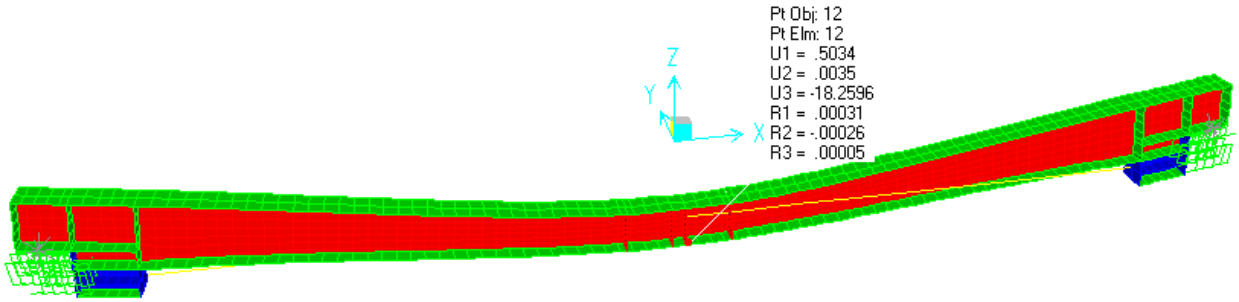

Displacement values in directions; U1: X, U2: Y, U3: Z.
Rotations around the related axis; R1, R2, and R3.

Fig. 14. Beam displacements (mm).

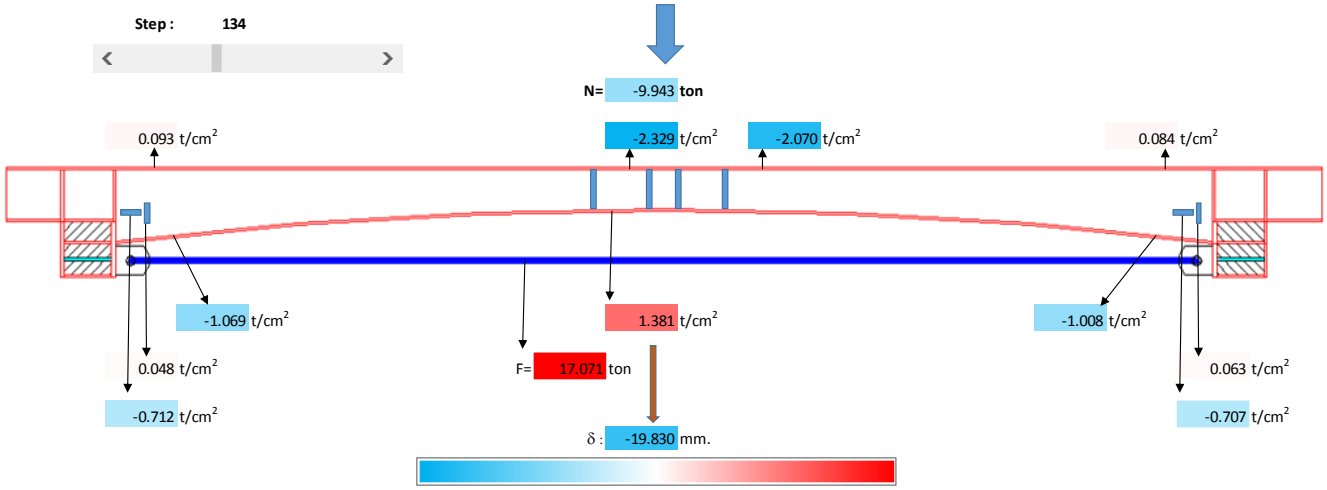

Fig. 15. Beam stress and displacement test results.

As can be seen, the stresses (at the mid-point 2.32 ≅ 2.35 t/cm²), displacement (19.83 ≅ 18.26 mm), and cable forces (17.07 ≅ 17.87 t) were reasonably close to each other.

The results obtained from the accelerometers were subjected to a fast Fourier transform (FFT) so that the cable forces could be calculated in terms of frequency (Fig. 16).

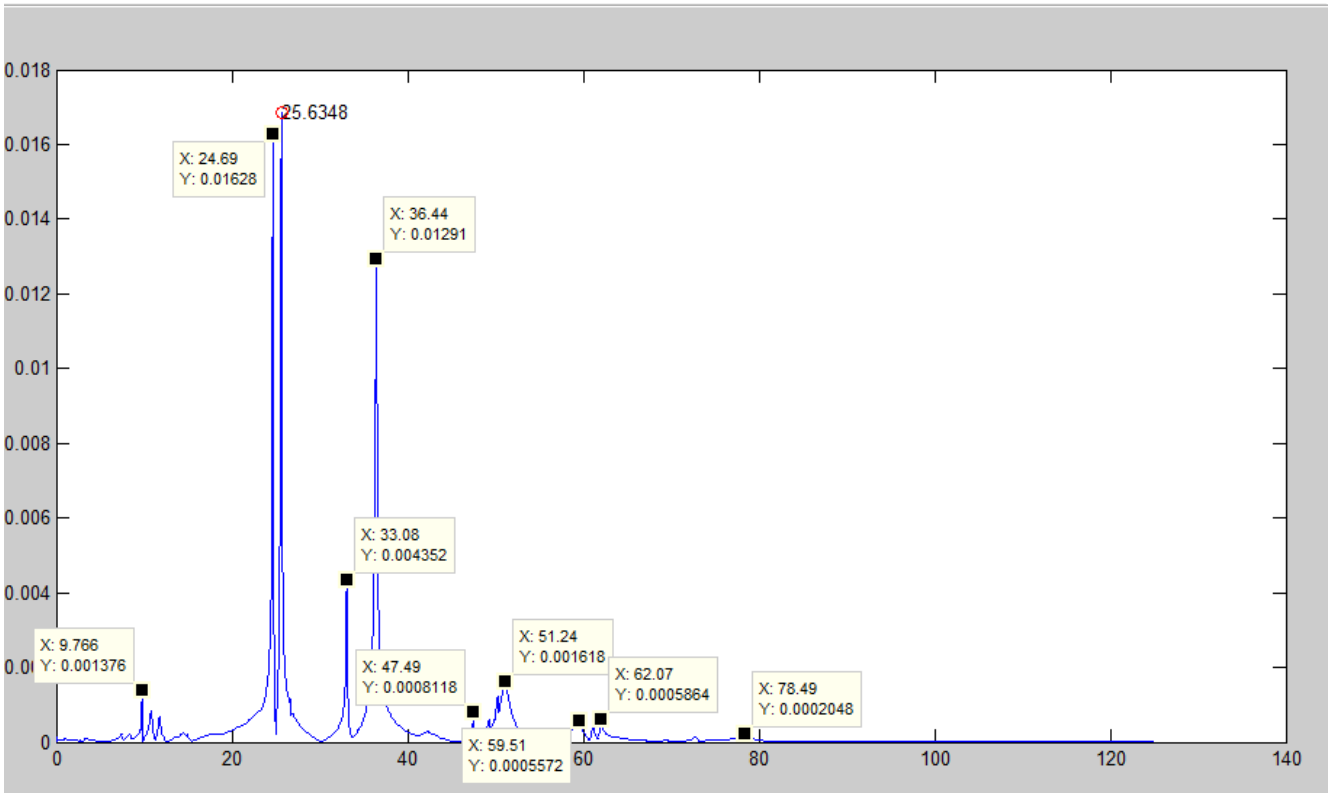

Fig. 16. Cable accelerometer FFT results for Test 4. Cable force = 16.9 t.

At 26.63 Hz, nearly all of the FFT results could be observed, so it was understood that this was the frequency of the systems and was consequently ignored. When all of the FFT results were compared, it is noticeable that between 27.16 Hz (Cable force 10.17 t) and 39.95 Hz (Cable Force 23 t), the frequencies changed due to the cable forces. Therefore, it is understood that the cable frequency was 36.44 Hz (Cable Force 16.9 t). Table 1 contains a detailed comparison in which all of the close FFT frequencies are presented one under the other; variable frequencies were chosen according to cable forces.

Vertical and horizontal accelerometer results were at the same frequencies as the cables.

$$T = 4\pi^2 ml^2 \frac{f_n^2}{\gamma_n^2} - \frac{EI}{l^2}\gamma_n^2 , \tag{5a}$$

$$\gamma_n^2 = n\pi + A\psi_n + B\psi_n^2 , \tag{5b}$$

$$A = -18.9 + 26.2n + 15.1n^2\ ,\ B = \begin{cases} 290 & (n = 1) \\ 0 & (n \geq 2) \end{cases}\ , \quad (5c)$$

$$\psi_n = \sqrt{\frac{EI}{m\omega_n^2 l^4}}, \quad (5d)$$

where;
T : Cable tension force
n : Mode number
ω_n : Angular frequency
E : Elastic modulus
m : Mass
l : Cable length
I : Moment of inertia

Table 1. Comparison of FFT results.

TEST -4 Force (t)		Frequency							1.Mod					2.Mod	
10.17	Cable		8.42	18.2	22.09	25.65			27.16	38.38	42.88	50	53.16	64	
	Horizontal					25						50			
	Vertical		8.42	19.56	22.09	25.7				38.36					
11.07	Cable		8.04	15.87	22.51	25	26.9		28.12		44.31	49.97		65.14	
	Horizontal					25							50		
	Vertical		8.04	15.87	22.5		26.93			39.9					
12	Cable	5.53	8.2	16.2	23.28	25	27.72		28.9	37.98	41.28		51.3	68.9	
	Horizontal	5.55	8.2	16.2					28.3				51.16		
	Vertical		8.2	16.2	23.27		27.74		28.3		41.28			63.37	
12.9	Cable		8.71	16.48	24.08		28.78		29.88		42.6		52.43		70.47
	Horizontal		8.71	16.48			28.79						52.51		
	Vertical		8.71	16.46	24.09		29.17				42.6			66.57	
14.1	Cable		9.95		24.92		28.72		32.98		44.22		57.31		72.79
	Horizontal		9.95				28.67		32.99		46.88				
	Vertical		9.95		24.92				32.99		44.22		57.13	66.6	
15	Cable		9.95			25.67	29.14		33.2		45.4				74.64
	Horizontal		9.95				29.31		33.23		48.39				
	Vertical					25.67	29.15		33.23		45.39				
15.9	Cable		9.74	15.56	24.1	25.36	26.18		34.12		46.46	49.58	58.94		76.1
	Horizontal		9.76		24.12	25.35		32.93	33.77		49.55		54.02		
	Vertical		9.77		24.09	25.36	29		34.07		46.45	49.58	53.94	58.88	
16.9	Cable		9.77		24.7	25.63		33.08	36.44				51.24		78.44
	Horizontal		9.77		24.67	25.65		33.09	36.44				51.06		
	Vertical		9.77			25.65	29.07	33.1	36.45		47.47				
18.2	Cable	5.74	9.77		24.87	26.15									80.2
	Horizontal	5.74	9.77		24.87	26.15	27.34	33.13	37.38				51.9	60.46	
	Vertical	5.74	9.77		24.87	26.15		33.14	37.4		48.97		51.99	60.44	
19.2	Cable		9.7	11.39	24.92	26.55	27.73		37.93				53.1	60.91	81.7
	Horizontal	5.49	9.7		24.91	26.56		33.04	37.92				52.53	60.76	
	Vertical		9.7	19.98	24.93	26.55	27.71	33	37.93			50	52.54	60.97	
20.2	Cable		9.7	11.54	24.95	26.99	29.95	33.02	38.51				53.96		85.63
	Horizontal	5.7	9.7		24.93	26.99	29.95	33.02	38.5				53.15		
	Vertical		9.7		24.96	26.99	29.97	33.02	38.5			51.06	53.21	61.46	
21.2	Cable		9.62	11.63	24.96	27.45	30.43	33	39.05				53.65	62.54	87
	Horizontal	5.76	9.63			27.45	30.43	33	39.07				53.7	62.4	
	Vertical	5.75	9.64	20.21	24.97	27.45	30.44	32.9	39.08				53.71	62.62	
21.9	Cable		9.61	11.7	24.97	27.68	30.71		39.36				53.35	62.92	87.75
	Horizontal	5.75	9.61			27.68		32.98	39.38				54.01		
	Vertical		9.61		24.99	27.68	30.72	32.98	39.36			52.69	54	62.74	
23	Cable		9.54	21.3		28.07	31.3	32.97	39.95				54.61	63.96	89.02
	Horizontal	5.74	9.54			28.08	31.3	32.96	39.96				54.6		
	Vertical		9.54	20.13	24.98	28.09	31.31	32.96	39.95				54.5		

Accordingly, the calculated cable force was 17.25 t, which was very similar to the strain gauge results (16.9 t).

Five sample test results are given in Fig. 17. Eqs. (3), (4) and (5) results were compared with the strain gauge results, from which the closest results were obtained with Eqs. (4) and (5).

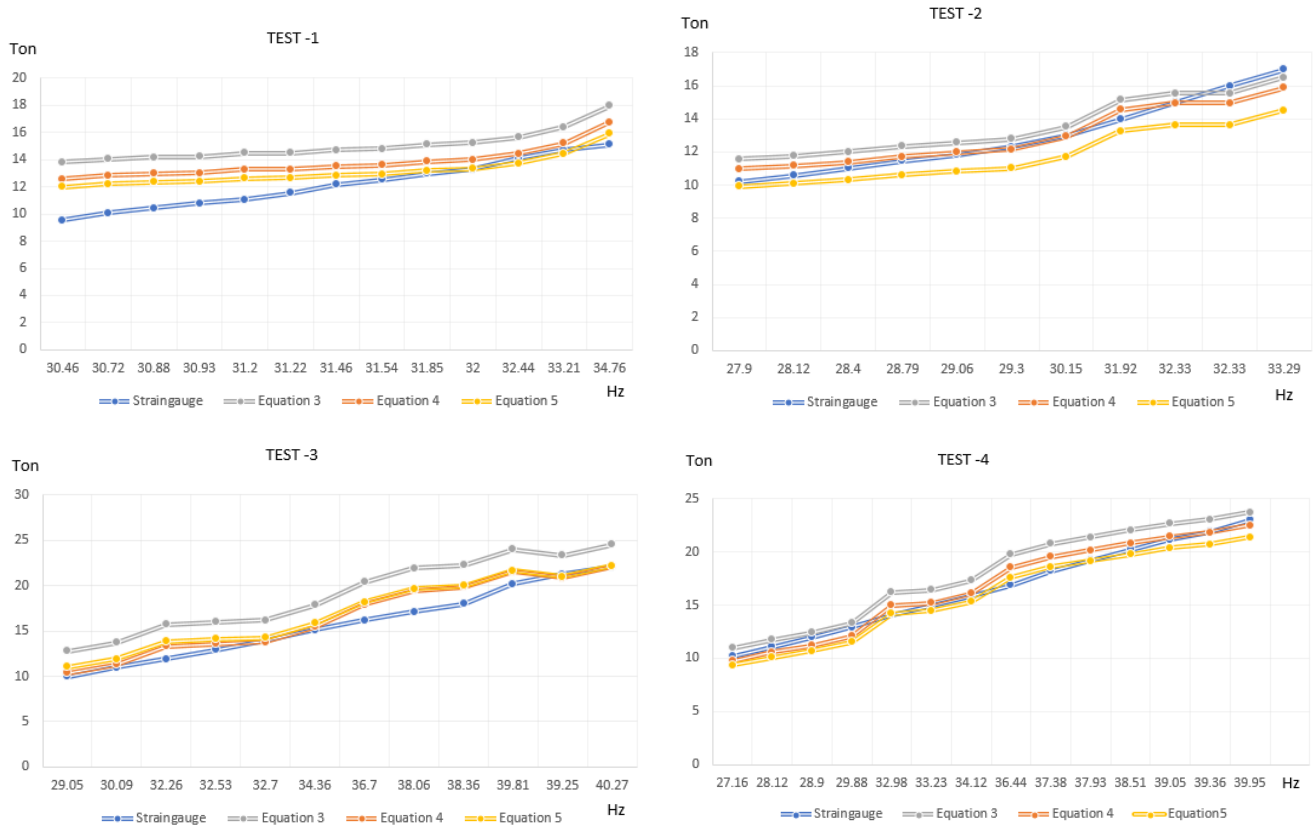

Fig. 17. Tests 1-4: cable forces - strain gauge results.

The equation results for the Test 1 start were quite different from the strain gauge results, which might have been because the accelerometer clamp was not fixed well to the cable. The other test results were in concert with the strain gauge results.

It was very difficult to see the second mode frequencies on the FFT graphics because they were very high and very close to the accelerometer progress up limits. The test second mode frequencies could be read more easily than the others could, and the closest results were found with Eq. 4, as can be seen in Fig. 18.

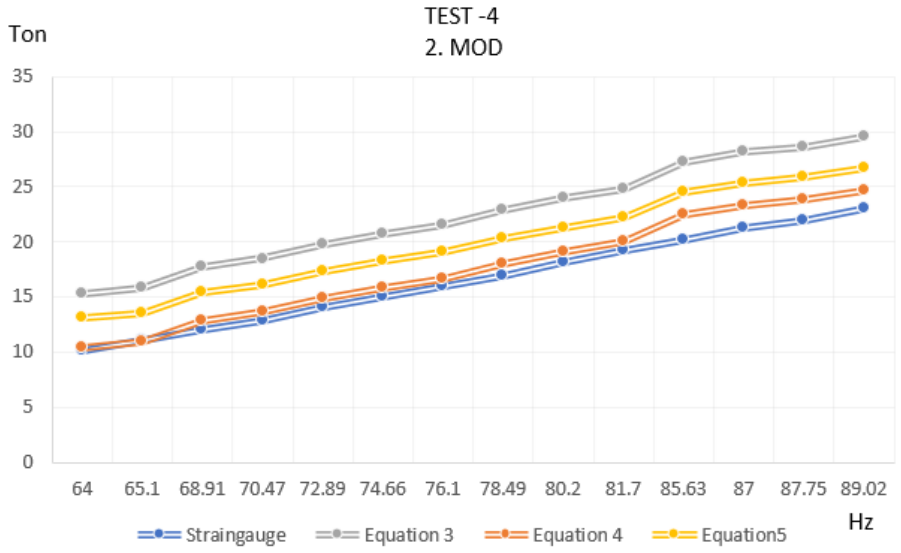

Fig. 18. Second mode: cable forces - strain gauge results.

The bearing capacity of the arch beam with a pre-tension cable was 15.5 t as opposed to 11.5 t without. Thus, as proposed in this study, it is obvious that when using arch beams with cables, the bearing capacity could be increased by 35%. All tests were finished whenever buckling of the beam flange occurred, as illustrated in Fig. 19.

Fig. 19. Buckling of a beam compression flange.

The buckling analysis was repeated for a single load during testing, the value of which was set at 7 t, to obtain the compression safety stress limit of the arch beam flange. Figs. 20 and 21 show the buckling mode characteristics for the conventional and arch beams, respectively.

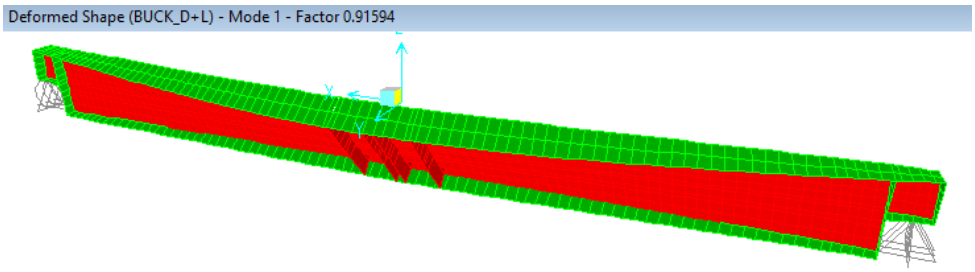

Fig. 20. Buckling mode of the conventional beam under a single load.

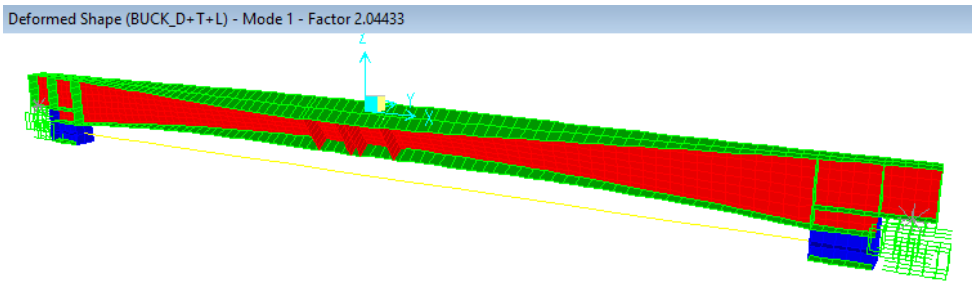

Fig. 21. Buckling mode of the pre-stressed arch beam under a single load.

Buckling mode factors were 0.91 and 2.04 for the conventional and arch beams, respectively. It is clear that 0.91 for the conventional beam was not sufficiently high as a safety factor and that 2.04 proves that the arch beam shape increased the bearing capacity of the beam considerably.

On the other hand, it might be possible to reduce flange stresses by increasing the cable tension force. Thus, it might be possible to obtain a higher load-bearing capacity for the beam proposed herein. The pre-tension force was increased up to 15 t and the finite element

analysis model of the beam was re-analyzed with the obtained stresses, as shown in Fig. 22.

In this case, the single load-bearing capacity was increased to 11.34 t (13.4%) and the pre-tension force was limited by the bottom flange compression safety stress. The 15 t pre-tension force generated 1.44 t/cm² compression stress at the bottom flange, which after the vertical loading, could be reduced by applying an additional pre-tension load to the cable. Thus, the system's maximum load bearing capacity could be increased much further with this method.

Temperature changes did not affect the system load or stress distribution by much at all. As an example, after applying a temperature increase of 5°C to the cable, the load change was only 230 kg and the stress difference was close to zero.

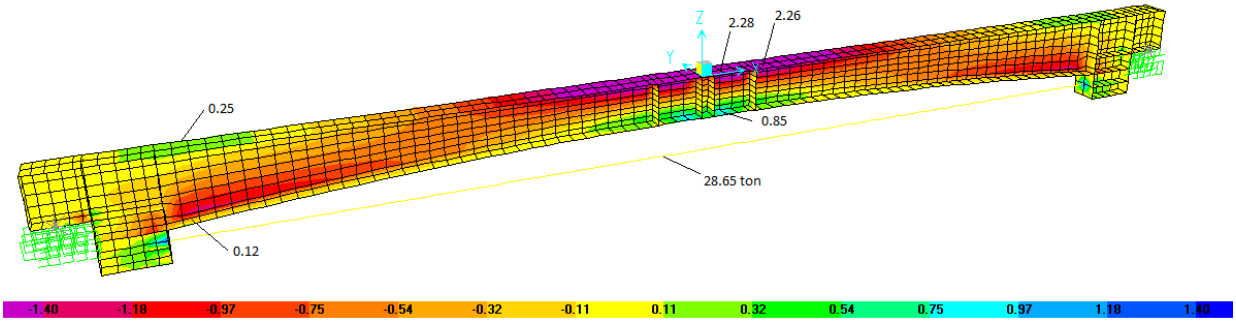

Fig. 22. Stress results for 15 t pre-tension force.

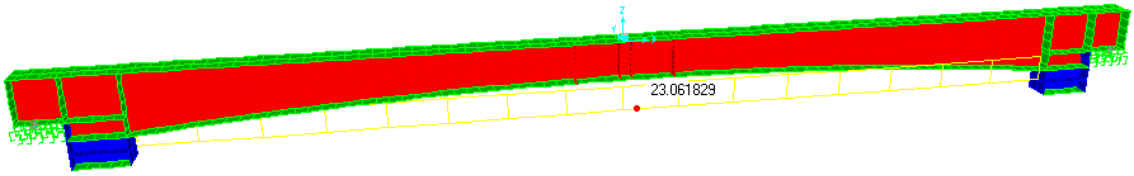

Fig. 23. The force on the cable before the temperature increase (load in tons).

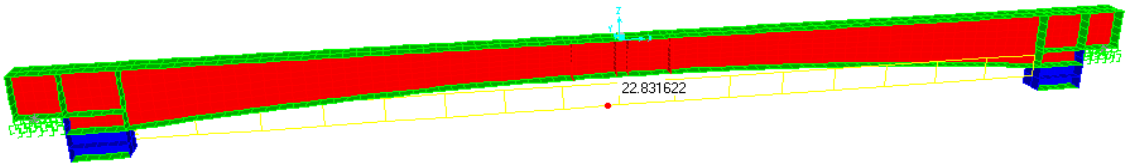

Fig. 24. The force on the cable after the 5°C temperature increase (load in tons).

The last beam test results with and without a cable are shown in Figs. 25 and 26, respectively. For the beam without a cable, only 4.18 t could be carried before reaching the safety stress level (beam failure without a cable is shown in Fig. 27). The load ratio was 7.11/4.18 =1.7, so the load bearing capacity with the cable increased by 70%.

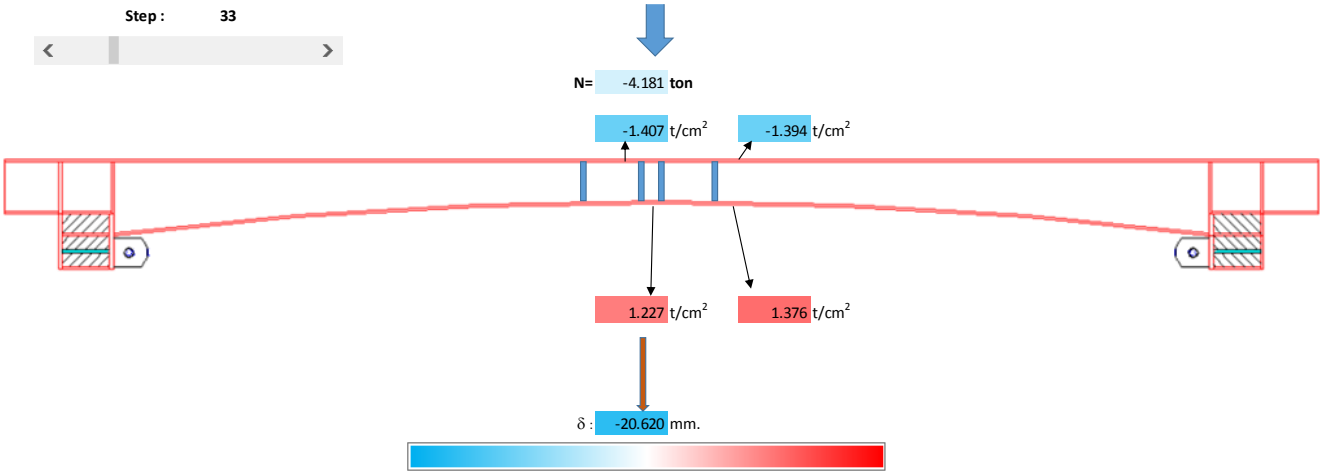

Fig. 25. Stress and displacement results for the arch beam without a cable.

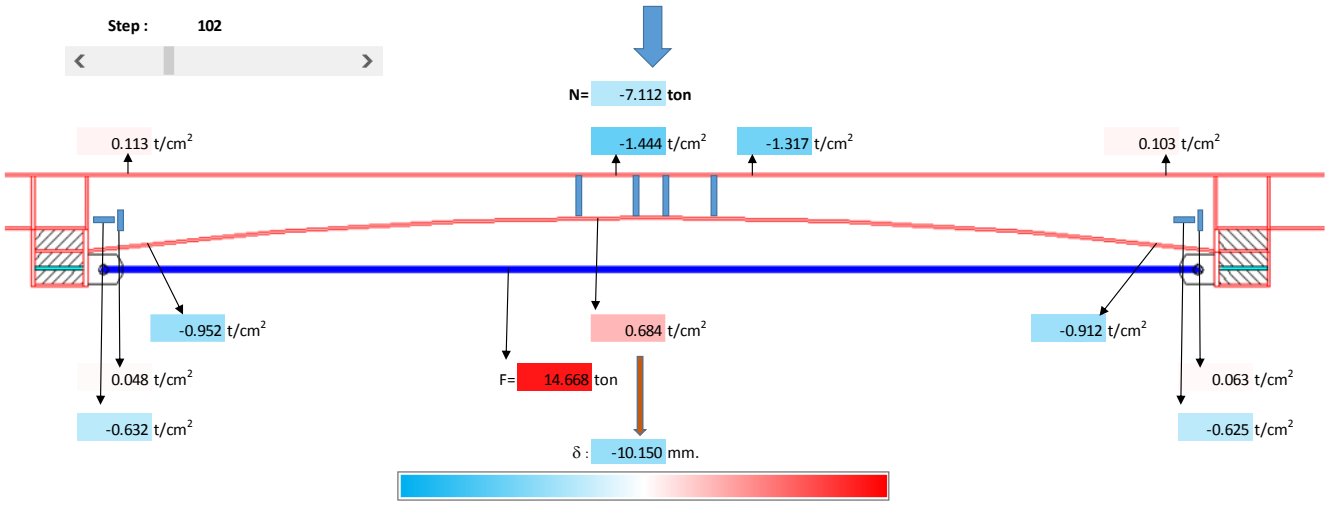

Fig. 26. Beam stress and displacement results for the arch beam with a cable.

Fig. 27. Test-5 beam (without a cable) after failure.

6. Conclusions

The load capacity of an arch beam supported by a pre-tension cable can be increased up to 2 times due to the fact that the compressive stress developed on the upper part of the beam is reduced by the adverse moment effect of the pretension force of the cable and decreasing the beam height at the mid-point of the span length causes an increase in the buckling load factor. There is no necessity for bracings to prevent lateral buckling of the top flange of the beam or for a reduction in beam height relative to the conventional hot-rolled beam section. This theory was proved by the buckling analysis. It was found that the bottom arch flange of the beam caused a delay in the buckling of the beam, which highlights a need to investigate new design methods to improve arch beam moment capacity.

The disadvantages of the proposed method are construction beam costs, cable pre-stressing, and stress losses that occur in the cable over time. However, the need for larger beams able to handle the same loads, the additional lateral joint elements required for beam stability, and the impact of these elements on the architectural appearance should actually balance or lower the overall costs. Moreover, the reduction of the pre-stressing force in the cable over time does not exceed 8% (Arda and Yardimci, 2000) and the temperature difference between the beam and cable should not be considered as a significant disadvantage.

The ease of passage of mechanical and electrical installations through the gap created by the belt shape of the beam which contemporarily gives a more architectural aesthetic appearance can be considered as a major advantage of arch beams supported by pre-tension cables, as proposed in this study. It is clear that when there is a sliding support structure, the simply supported system will not be affected by small temperature changes, and this ratio can be increased by adjusting the post-tension force on the cable if necessary.

REFERENCES

ANSI-AISC 360 (2010). Specification for Structural Steel Buildings. American Institute of Steel Construction (AISC), Chicago, USA.

Arda TS, Yardimci N (2000). Çelik Yapıda Öngerme. Birsen Yayınevi, İstanbul Turkey.

Humar JL (1990). Dynamics of Sstructures. Prentice Hall, New Jersey, USA.

IMO - 02/2008 (2008). Çelik Yapılar Hesap Kuralları ve Proje Esasları. Turkish Chamber of Civil Engineers (TMMOB/IMO), İstanbul, Turkey.

Wang ML, Chen ZL, Steve SK, George ML (2000). Magneto-elastic permeability measurement for stress monitoring in steel tendons and cables. *Proceedings of SPIE the International Society for Optical Engineering*, Vol. 3995, 492-500.

Zhi F, Jian-qun W (2012). Practical formula for cable tension estimation by vibration method. *Journal of Bridge Engineering*, 17(1), 161-164.

Challenge Journal of Structural Mechanics

Research Article

An investigation of the behavior of header end-plate connections under monotonic loading

Adem Karasu *, Cüneyt Vatansever, Haluk Emre Alçiçek

Department of Civil Engineering, İstanbul Technical University, 34469 İstanbul, Turkey

ABSTRACT

In seismically active regions such as Turkey, the context of the nonlinearity provided by a building is based on the behaviors of structural components; beams, columns and their connections constituting the seismic force resisting system of the structure. Of these members, beam-to-column connections can play a considerably important role even if they have a capability of limited stiffness and flexural strength. Structural steel connections are mainly classified as a pinned or a moment connection. However, some beam-to-column connections having limited stiffness and flexural strength, which are called semi-rigid connections such as header end-plate connections designed so as to transmit only shear forces, can be characterized by moment-rotation relationship. This paper investigates the behavior of header end-plate connections using finite element (FE) modeling. The FE models include material, geometrical and contact nonlinearities. FE modeling technique was first verified through the test results of the experimental research performed by Aggarwal (1990). Then the effect of header end-plate thickness upon moment-rotation relationship was investigated. According to the analyses results, in addition to shear stresses, axial tensile stresses have been observed to occur in the bolts at the tension side and thickness of the header end-plate and beam web play a governing role in the development of initial rotational stiffness and the flexural strength of header end-plate connections.

ARTICLE INFO

Article history:
Received 27 June 2018
Revised 23 July 2018
Accepted 2 August 2018

Keywords:
Header end-plates
Semi-rigid connections
Finite element models
Moment-rotation relations

1. Introduction

Due to unexpected brittle failure of welded beam-to-column connections during the 1994 Northridge earthquake, researcher have raised investigations on moment resisting beam-to-column connections to sustain their ductility during earthquake. Semi-rigid beam-to-column connections have also been studied since they have exhibited ductile behavior if designed in such a way that plastification due to plate bending has dominated the energy absorption in the connection. Experimental and analytical studies showed that semi-rigid beam-to-column connections could have sufficient rigidity, ductility and strength. Moreover, these connections exhibited more suitable results than rigid welded connections (Chen et al., 2011). In designing a steel framework, it is customary to represent the connection behavior as a fully moment resisting connection or a simple connection. However, this approach leads to an inaccurate prediction of the frame behavior because perfectly rigidity and complete flexibility are idealized forms of connection behavior and cannot be reached in practical connections. In particular, the behavior of lateral force resisting frames with semi-rigid steel beam-to-column connections cannot be accurately estimated under lateral forces when the moment-rotation relationship of the connections has not been considered. Therefore, if the semi-rigid connections are used, effects of the connection flexibility on the frame behavior must be taken into account in the design procedures. The primary parameter of the steel beam-to-column connections is their rotational deformation, θ_R caused by the in-plane bending moment, M (Fig. 1) (Abdalla and Chen, 1995). The shear and axial deformations of the connections are generally ignored.

* *Corresponding author*. Tel.: +90-212-2853800 ; E-mail address: karasuad@itu.edu.tr (A. Karasu)
ISSN: 2149-8024 / DOI: https://doi.org/10.20528/cjsmec.2018.03.004

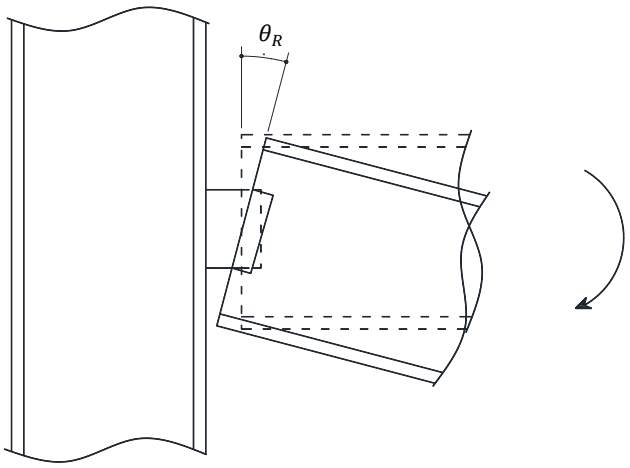

Fig. 1. Rotational deformation of the connection.

In the design of header end-plate beam-to-column connections only shear force has been considered as they are assumed to be pin-connected. However, these types of connections may have a considerable, but limited, flexural strength, and can be rigid enough to provide a contribution in lateral stiffness of the frames, which is influenced by end-plate thickness, bolt diameter and bolt arrangement. In order to account for this contribution for design purposes, moment-rotation relationship of header end-plate beam-to-column connections has to be defined. In fact, tensile stresses in the bolts at the tension side of the connection, in addition to shear stresses, should be taken into consideration during the design procedure (Karasu and Vatansever, 2017).

The aim of this paper is to investigate the behavior of header end-plate beam-to-column connections under monotonically increasing load. These types of connections consist of an end-plate whose height is smaller than the beam depth and bolts arranged as shown in Fig. 2. End-plate (header plate) is welded to the beam web and bolted to the column flange. The importance of these connections in the context of overall structural behavior lies in their rotational stiffness. Actually, they are assumed to be pinned flexible connections during the design procedures although they have pronounced rotational stiffness. Behavior of the header end-plate connections can be defined by moment-rotation relationship obtained by experimental tests, analytical models, numerical models and FE models. The most confidential results can be achieved by experimental tests. However, due to cost of experimental test, one of the other methods alternative to the experimental study can be utilized. In this paper, FE modelling technique which was first validated through a comparison of moment-rotation curves from experimental research performed by Aggarwal (1990) has been used to obtain the behavior of header end-plate connection. By taking the experimental conditions into considerations, such as material properties and contact conditions, the FE model has been developed. The test setup and member details considered are shown in Fig. 3.

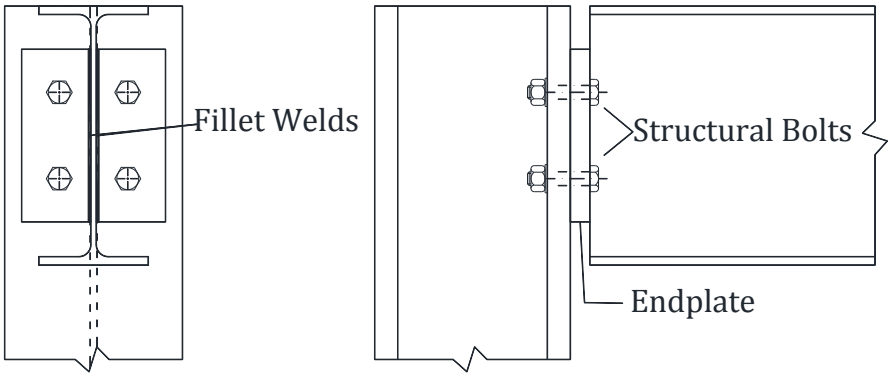

Fig. 2. Components of header end-plate connection.

For the header end-plate connections, collapse mechanism typology is related to the ratio between the flexural strength of the header end-plate and axial strength of the bolts (Faella et al., 2011). Additionally, beam web yielding and beam web local buckling are also limit states for the connection in bending. However, premature web local buckling must be avoided as it causes a brittle failure. This can be ensured that the flexural rigidity of header end-plate should be less than the axial rigidity of beam web. If this is warranted, ductile behavior is also provided.

Tensile stresses in the bolts at the snug tight condition may reach a high level, resulting in a decrease in the shear strength of the bolts. In order to avoid premature bolt failure due to tension forces from bending and prying forces, yield line mechanism should be developed in header end-plate before the strength of the bolts is exceeded. To guarantee the yield line mechanism in the header end-plate, pretension can be applied to the bolts. This paper also investigates the variation of axial stresses in the bolts preloaded up to 70% of their tensile strength. To better understand the yield line configuration, FE analyses have been performed to observe the failure mechanisms of the connection models with different end-plate thicknesses.

The studies on header end-plate connections have concentrated on experimental tests and analytical studies for achieving the moment-rotation relations (Sommer, 1969; Aggarwal, 1990; Pilgr, 2009). In the study conducted by Sommer (1969), twenty tests have been

performed to observe the effects of the end-plate thickness, bolt diameter and bolt orientation on the moment-rotation relations. Aggarwal (1990) has carried out some tests on header end-plate connections with two different end-plate configurations. Pilgr (2009) has performed experimental tests to observe moment-rotation relations.

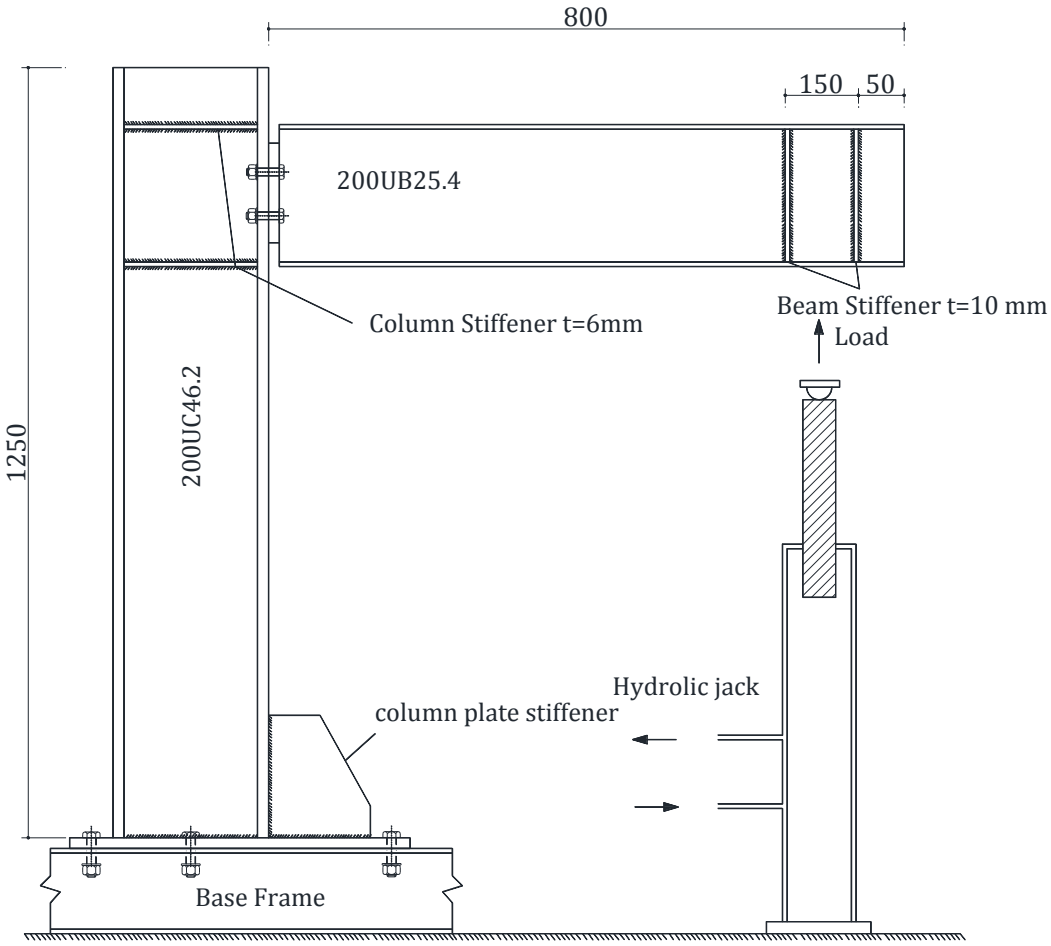

Fig. 3. Test setup for specimen M3 (adopted from Aggarwal, 1990).

2. Verification of Finite Element (FE) Modelling

Before FE models of the header end-plate connections considered in this study, FE modelling technique has been verified through the results of experimental research conducted by Aggarwal (1990). For the verification, the results from the test of the specimen M3 has been taken into account and its FE model has been developed. The model includes material and geometrical nonlinearities. Initial imperfection corresponding to appropriate buckling mode associated with the loading has also been accounted for with the scale value of $L_{BEAM}/1000$ (Ismail et al., 2016). Linear eigenvalue analysis is used to estimate the suitable buckling mode. Therefore, application of the imperfection becomes possible to trigger buckling of the beam web within the connection. Riks method is used for nonlinear analysis of the connection.

In order to simulate the test setup, the column is assumed to be fixed at the bottom and the lateral displacement of the column is prevented. A point load was applied to tip of the beam which is allowed to deflect upward in the same manner as in the test. Lateral displacement of the beam was restrained to prevent any possibility of premature failure caused by lateral torsional buckling.

The specimen considered consists of a beam 200 UB 25.4 with 12mm thick end-plate attached to the beam web with fillet welds and connected to the flange of the column 200 UC 46.2 with four M20-10.9 bolts. All the bolts are pretensioned to the minimum specified pretension force defined as 70% of the bolt tensile strength. The yield stress considered for the material of beam, column and end-plate is 250 MPa. The yield and ultimate stress for the bolts were taken as 900 MPa and 1000 MPa, respectively. Joint details are given in Fig. 4. Each material for each member was defined by true stress-true strain curve. Therefore, engineering stress-strain values were converted to true stress-strain values (Kaufmann et al., 2001).

2.1. Element properties

3d FE model corresponding to the specimen of M3 is given in Fig. 5. The connection model is developed by using a general commercial program ABAQUS. The model includes material and geometrical nonlinearities, and also nonlinear interaction between the surfaces in contact to each other. All bolts in the connection are tightened with the sufficient pretension. For more reliable

performance, the eight-node brick elements C3D8I with incompatible modes are used. Since having additional degree of freedoms, C3D8I has a capability to capture bending behavior better. By using this element type, shear locking which leads to observe stiffer behavior for bending behavior due to getting shear deformations instead of flexural deformations, is removed and volumetric locking is much reduced.

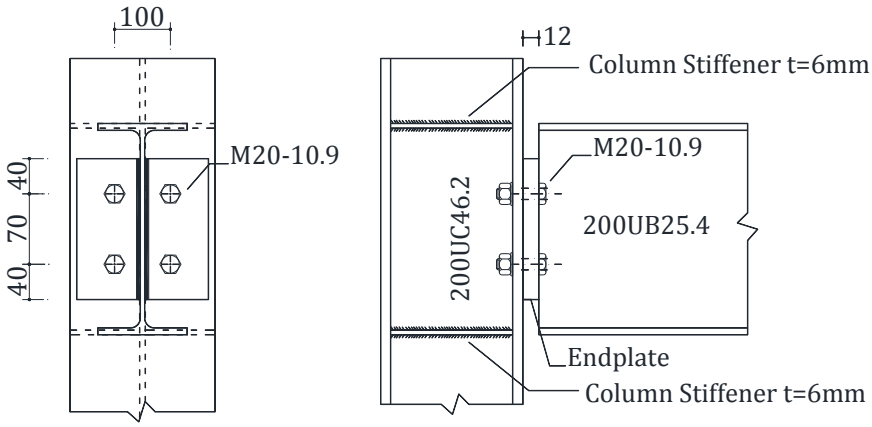

Fig. 4. Details of the header plate connection.

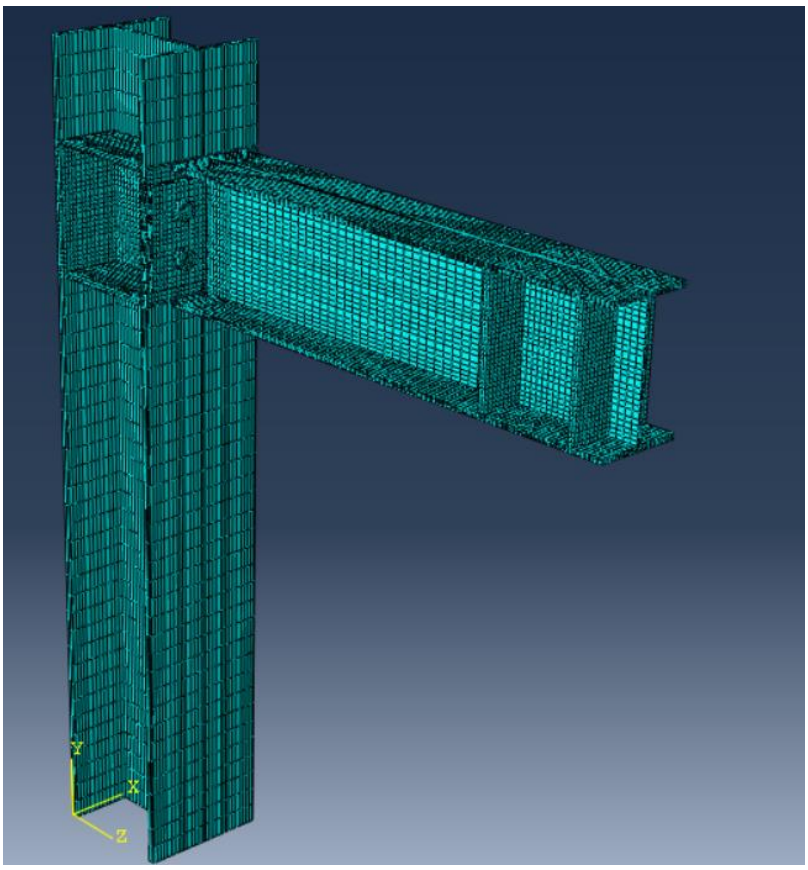

Fig. 5. 3D FE model in ABAQUS.

2.2. Contact interaction properties

One of the most important process for the FE modelling is to reflect the contact interaction properties into the models properly. If this type of interaction is improperly modeled, it is not possible to simulate the behavior of the connection in a realistic manner. Modelling the contact interaction; between the outer surfaces of the column flange and header end-plate and between the bolt head/nut and column flange/end-plate requires two different interaction properties to define. First one is 'hard contact' property assuming that when the surfaces are in contact, any contact pressure can be transmitted between surfaces. However, if the contact pressure is zero, the surfaces are separated. The second one is tangential behavior of the contact. In this definition, friction between the contact surfaces at the connection is modelled using the classical Coulomb model where the friction

coefficient is 0.30 (Ismail et al., 2016) by using penalty stiffness formulation. It is also allowed to small sliding effects at the interface of the contact surfaces. Welding connection between the header end-plate and beam web is modelled by tie constraint.

For the simulation of header end-plate connection, in addition to static and implicit solver, explicit dynamic solver is also suggested due to complicated contact problems. For the static and implicit analyses for each load increment, the continuity of the contact state is checked first and if there is any change on the contact state, general stiffness matrix is calculated on the new changed contact state. Therefore, it will be difficult to find the changed contact state when there are too much contact interactions in the model that leads to convergence difficulties for the both static and implicit solver. In the quasi-static explicit dynamic solver, kinematic contact was used. According to this algorithm, at first model predicts the configuration of the deformed shape without contact conditions. Then the equilibrium state is determined to calculate time increment and resultant force to remove the penetration of the slave nodes on the master surfaces. In the quasi-static explicit analyses, the ratio of kinetic energy to internal energy must be smaller than 1% throughout all loading steps (Hongxia et al., 2007). This can be ensured by reducing the mass scaling, but which increases the computational time.

2.3. Meshing

Another important issue in the FE modelling is element meshing that governs the accuracy of the analysis results. For accurate results with less computational time, different mesh sizes have been assigned to each FE model part, i.e. a finer mesh in the vicinity of the connection where high stress and strain gradients are assumed to take place was used, while the coarser mesh was employed in the areas far from the connection zone. Also, to get acceptable results under flexural moment, at least four layers were formed through the member thickness. Meshing of each component considered in the model are shown in Fig. 6.

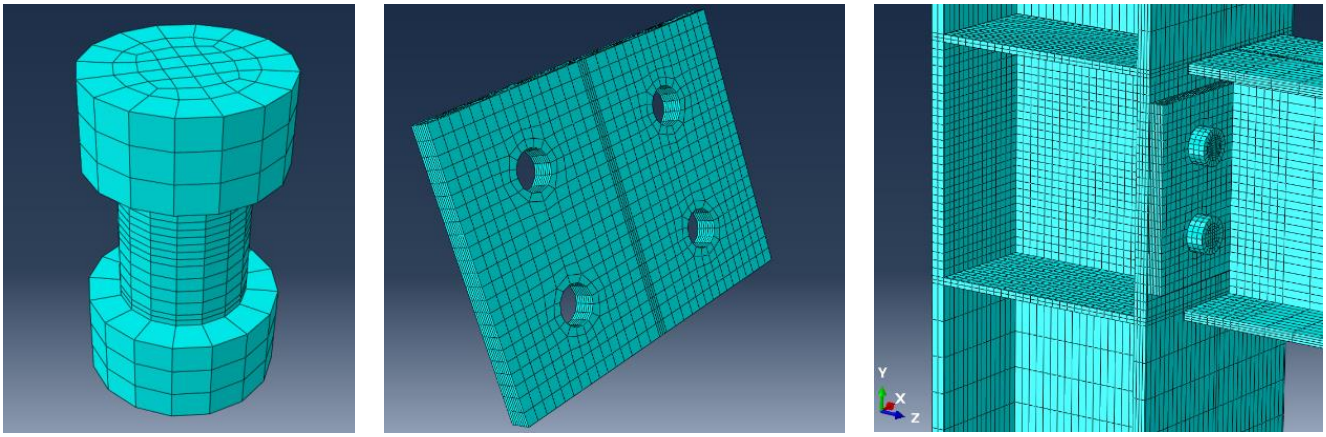

Fig. 6. Meshing of different components in the model.

2.4. Loading

The FE analyses of the model involved two load steps. The first load step was used to apply pretension forces to the bolts by applying displacements to the ends of the bolt heads. The prescribed bolt displacements corresponding to the axial force of 172 kN (TCDCSS, 2016) which is defined as the minimum pretension force for M20-10.9 bolts were calculated considering axial rigidity of the bolts. The second load step was employed to define monotonic loading path applied by imposing upward displacement to the free end of the beam.

2.5. Parametric study

A parametric study was carried out to examine the effect of header end-plate thickness upon the response of the four-bolt header end-plate connections. The thicknesses were chosen to vary from 8 to 16 mm.

3. Comparison of the Moment-Rotation Curves

Analysis results from two different models were compared with experimental data in terms of moment-rotation characteristics, load carrying capacity and the failure mode of the connection. As shown in Fig. 7, the analysis results are in good agreement with those from the experimental test. Both results from experimental test and FE analyses support that the end-plate flexural deformation and yielding of beam web govern the flexural moment capacity of the joint. Deformed shape of the connection and plastic regions occurred at the end of analyses are shown in Fig. 8. The load carrying capacity which is obtained as 32 kN (Chen et al., 2011) also estimated with good accuracy.

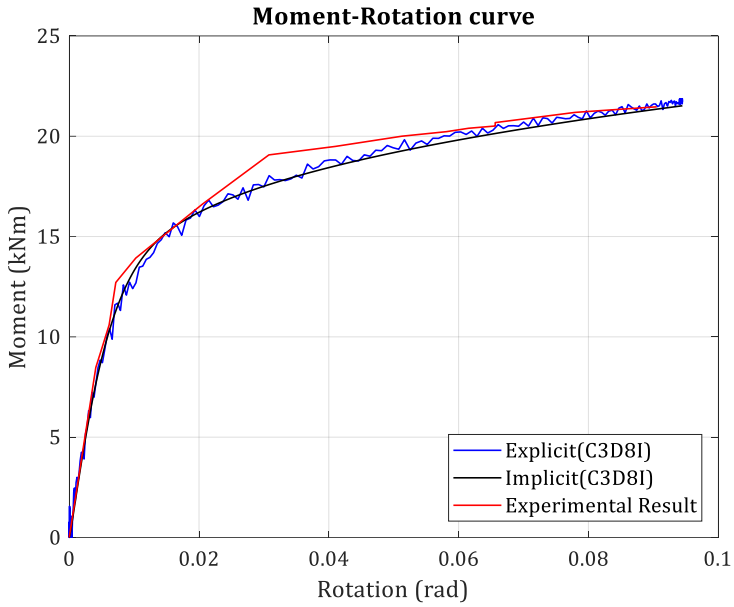

Fig. 7. Moment-rotation relationship.

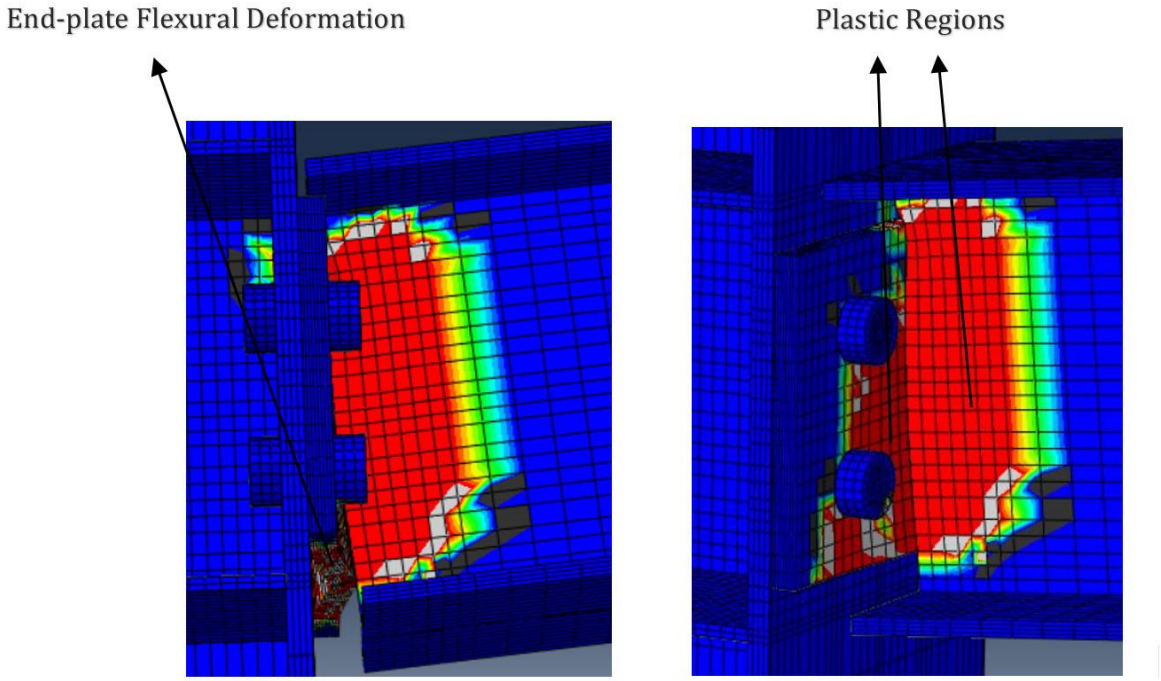

Fig. 8. Deformed shape and plastic regions of the connection.

4. Analysis Results

Analysis results have shown that pretension applied to the bolts influenced the initial response of the connection. For the explicit dynamic analyses, it was observed the minor vibrations in the elastic and inelastic part of the moment-rotation curve due to loading speed effect. Depending on the bolt diameter and the thicknesses of header end-plate and column flange, bolts may exhaust their strength if the tensile stresses in bolts reach a sufficiently high value before a yield mechanism in the header end-plate develops (Jaspart and Demonceau, 2008). To observe the variation of the axial stresses (S33) in the bolt shank is therefore shown in Fig. 9. Based on the implicit analyses results, since the most stressed region was quarter part of the cross-section at the mid-length of the bolt shank, this region was considered to obtain the variation of axial stress shown in Fig. 10. In this figure, axial stresses were calculated by taking the average of axial stresses on the nodes within the region. It was observed that the axial stresses decreased about 300 MPa that is equal to 30% of the tensile strength of the bolt. Nevertheless, clamping force, which is provided by pretension applied to the bolts, to keep the header end-plate attached to the column flange was not beaten. Furthermore, this allows the yield mechanism to develop in the header end-plate or the column flange, whichever is the governing.

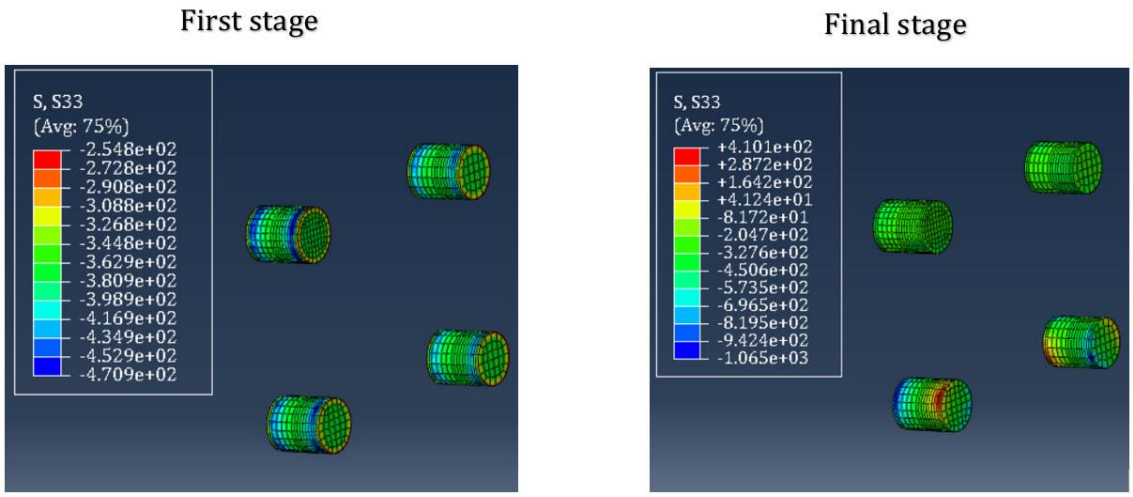

Fig. 9. Bolt axial stresses S33 for the first and final stage of the loading.

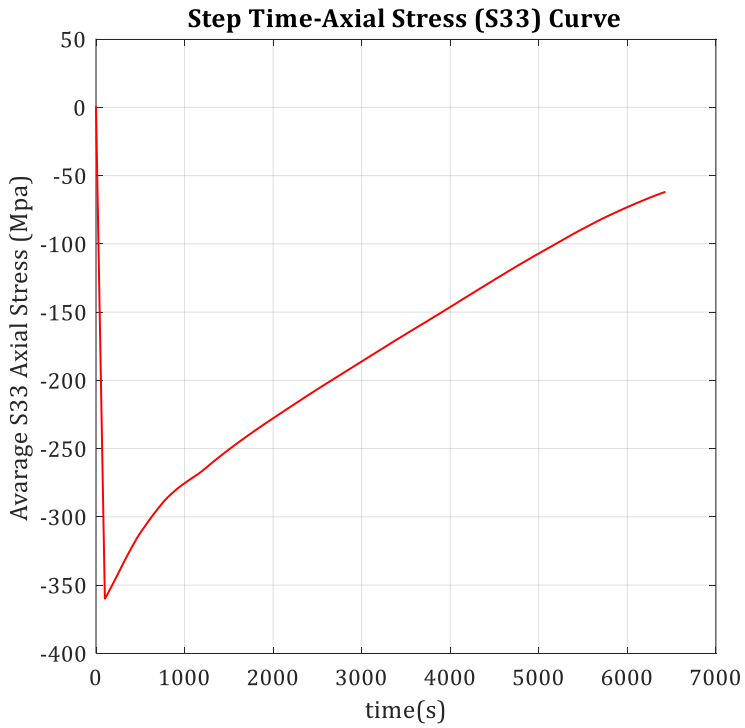

Fig. 10. Variation of axial stresses S33 in the bolt shank (avg.).

Analysis results show that the header end-plate thickness has an important role in determining the behavior of the connection. The plastic regions (indicated by red color) of the beam side for different thicknesses were given in Fig 11. The header end-plates with the thickness larger than 16 mm can be considered as a non-energy dissipative element in the context of this study because they have no a considerable contribution to the energy dissipation. Instead, the beam web yielding and its post-buckling behavior seem to be pronounced. Moreover, it is clear that thicker end plates, which means the plates having higher rigidity, increase the initial rotational stiffness and cause less or no praying force when the Figs. 11 and 12 are examined.

5. Conclusions

A series of 3D FE analyses was conducted to investigate the behavior of header end-plate connection using a general purpose of FE software, ABAQUS. In the study, header end-plate thickness was selected as a parameter. According to the analyses results, the connections with relatively thin end-plates have reached the flexural capacity with the plastification of end-plates and beam webs while the post-buckling of the beam web together with yielding was dominant in the others. Since the post-buckling behavior of beam web causes the strength degradation this phenomenon should be avoided. Based on the analysis results only, the ductility of the connection

was found to be acceptable for all connections. However, an experimental research is still needed for further evaluation on the ductility. As long as the thinner end-plates were employed, praying forces which increase the tensile stresses in the bolts became more pronounced. Also, the bolts remained elastic during the analyses. Nevertheless, based on the variation of the axial stress in bolts, it should be taken into account in the design of the bolts. Finally, although header end-plate connections have a limited flexural stiffness and strength, they seem to be promising to provide additional energy dissipation which is essential for better performance of seismic force resisting systems.

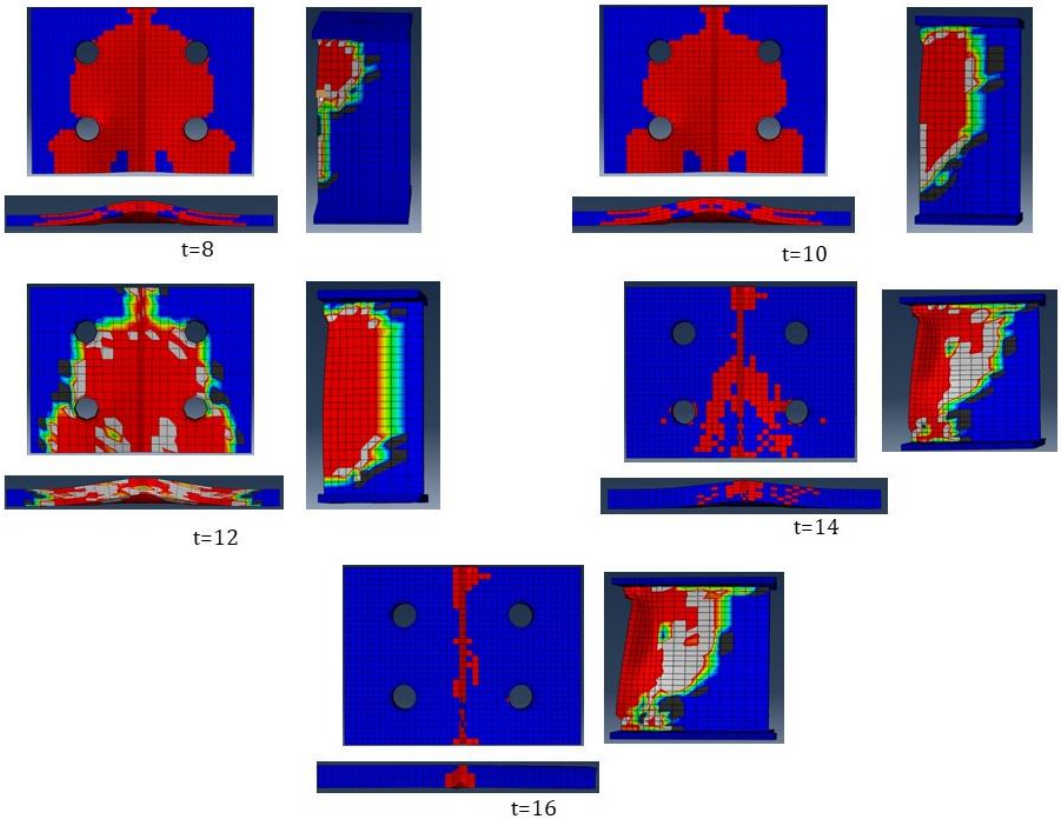

Fig. 11. Plastic region propagation in header end-plate and beam web.

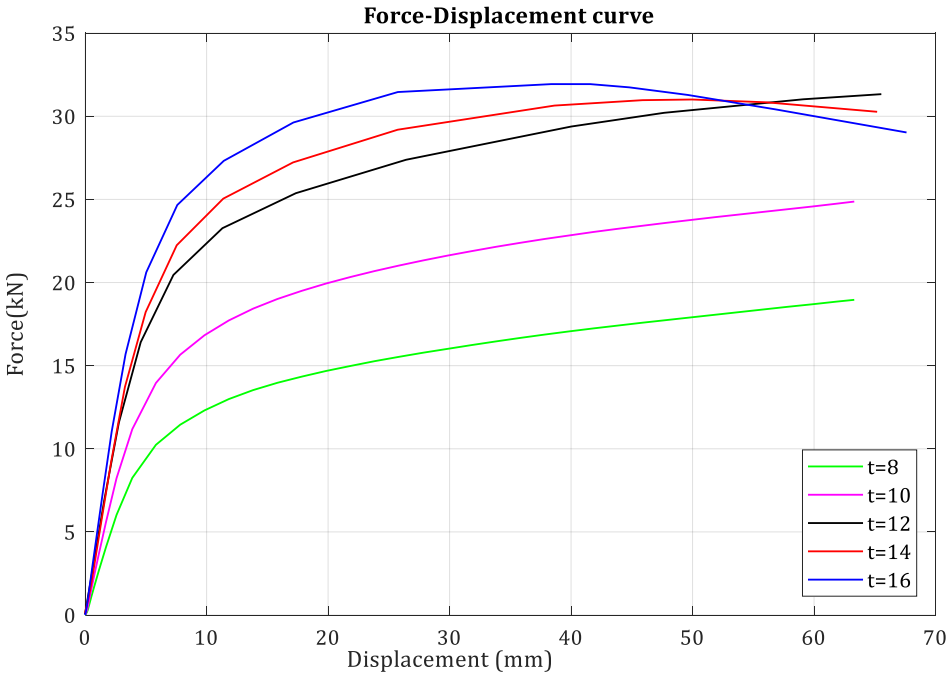

Fig. 12. Effect of header end-plate thickness on the connection behavior.

REFERENCES

Abdalla KM, Chen WF (1995). Expanded database of semi-rigid steel connections. *Computers and Structures,* 56(4), 553–564.

Aggarwal AK (1990). Behaviour of flexible end plate beam-to-column joints. *Journal of Constructional Steel Research,* 16, 111–134.

Chen W, Kishi N, Komuro M (2011). Semi-Rigid Connections Handbook. J. Ross Publishing, USA.

Faella C, Piluso V, Rizzano G (1999). Structural Steel Semirigid Connections. CRC Press LLC, USA.

Hongxia Y, Burgess IW, Davison JB, Plank RJ (2007). Numerical simulation of bolted steel connections in fire using explicit dynamic analysis. *Journal of Constructional Steel Research,* 64(5), 515-525.

Jaspart, JP, Demonceau, JF (2008). European design recommendations for simple joints in steel structures. *European Convention for Constructional Steelwork.*

Ismail RES, Fahmy AS, Khalifa AM, Mohamed YM (2016). Numerical study on ultimate behavior of bolted end-plate steel connections. *Latin American Journal of Solids and Structures,* 13(1), 1–22.

Karasu A, Vatansever C (2017). Nonlinear behavior of header end-plate connections under increasing monotonic loading. *7th international symposium on steel structures,* Gaziantep, Turkey. (in Turkish)

Kaufmann EJ, Metrovich B, Pense AW (2001). Characterization of Cyclic Inelastic Strain Behavior On Properties of A572 Gr. 50 and A913 Gr. 50 Rolled Sections. ATLSS Report No 01-13, Lehigh University, Bethlehem, USA.

Pilgr DM (2009). Experimental verification of actual behavior of header plate connections. *The Nordic Steel Construction Conference.*

Sommer WH (1969). Behaviour of Welded Header Plate Connections. *Master's thesis,* University of Toronto, Toronto, Canada.

TCDCSS (2016). Turkish code for design and construction of steel structures 2016, Ministry of Environment and Urbanisation, Ankara, Turkey.

Challenge Journal of Structural Mechanics

Research Article

Numerical investigation of reinforced concrete frame behavior subjected to progressive collapse

Mohammad Bagher Paripour *, Ahmet Budak, Oğuz Akın Düzgün

Department of Civil Engineering, Atatürk University, 25240 Erzurum, Turkey

ABSTRACT

Progressive collapse is defined as the spread of an initial local failure of a structure. This phenomenon, caused by the removal of one or more load-bearing element, is followed by a chain of failures through the structure and ultimately leads to partial or even full collapse of an entire structure. As a result, an accurate understanding of structural behavior subjected to large displacements, caused by progressive collapse, is essential to ensure a safe structural design. A progressive collapse in buildings often starts with the removal of one or more columns and continues with the collapse of adjoining structural elements. Experimental studies on progressive collapse are generally not recommended because of its cost and safety reasons. Today, as a result of progress in computer technology, more complicated problems can be investigated numerically. In this study, a numerical model is used for nonlinear analysis of a reinforced concrete (RC) frame behavior subjected to progressive collapse. It is obtained that there is a good agreement between the results with those of the experimental study given in the literature. According to the results, it can be predicted numerically the response of an RC frame to progressive collapse at a highly accurate level.

ARTICLE INFO

Article history:
Received 30 April 2018
Revised 23 July 2018
Accepted 10 August 2018

Keywords:
Progressive collapse
Reinforced concrete frame
Finite element analysis
Failure analysis

1. Introduction

In structural engineering, it is always aimed to predict some factors that significantly affect the durability and strength of a structure during its lifespan. These factors should be taken into account by the design engineer during the design process to ensure the structural stability under progressive collapse. The progressive collapse is defined as the spread of an initial local failure from element to element, eventually resulting in the collapse of an entire structure or disproportionately large part of it. The key characteristic here is that the total damage at the end is not proportional to the original cause (ASCE, 2016; Bažant and Verdure, 2007; Starossek, 2009). The first progressive collapse event which attracted engineers' and researchers' attention was the partial collapse of Ronan Point (a 22-story tower block) in 1968, initiated by a gas explosion in the 18th story, causing local progressive collapse of all stories (Pearson and Delatte, 2003). The final state of the collapse of the Ronan Point apartment building is shown in Fig. 1. The progressive collapse of Alfred P. Murrah Building in 1995 was another big event that attracted the second wave of attention (Corley et al., 1998). Due to the high mortality and economic losses from attacks on the twin towers of the World Trade Center (WTC) in 2001, progressive collapse once again attracted different entities to address this phenomenon more carefully and seriously (Reeve, 1999).

The National Building Code of Canada (NBCC) (2005) has set out the requirements for the design of principal elements, the connection of elements, and alternative load path methods. The ACI 318 (2014) imposes the structural integrity requirements to prevent entire structural collapse subjected to a local failure. The ASCE 7 (2016) provides a design method and a tool for determining the load combinations. It also addresses structural integrity such as ACI 318. Recently, the General Services Administration (GSA) (2003) and the Department of Defense (DoD) (2009) of the United States developed functional

* *Corresponding author*. Tel.: +90-539-2018550 ; E-mail address: mohammadbagher.paripour12@ogr.atauni.edu.tr (M. B. Paripour)
ISSN: 2149-8024 / DOI: https://doi.org/10.20528/cjsmec.2018.03.005

design guidelines to reduce the risk of progressive collapse. These guidelines present the alternative load path (ALP) method as the best technique to assess building vulnerability to progressive collapse. The dominant view in ALP is the use of alternative load path for handling gravity load in case of failure in the initial load path.

Fig. 1. Ronan Point apartment building after collapse (Pearson and Delatte, 2003).

Many studies have conducted investigations on the progressive collapse in recent years. Kaewkulchai and Williamson (2003) investigated a 2D model to compare the static and dynamic analyses of progressive collapse. According to their findings, the static analysis alone cannot represent the actual behavior of a structure subjected to progressive collapse. As a result, the dynamic behavior following the removal of the column has a significant effect in this regard. Iwankiew and Griffis (2004) investigated the progressive collapse mechanism in different structures and concluded that the architectural plan of a structure has a significant effect on its progressive collapse resistance performance. To obtain real results using static analysis, Ruth et al. (2006) proposed the use of increase factor of 1.5 for imposed loads. In addition, the relevant recommendations of these codes were compared. Bao (2008) developed 20 macro models to simulate the nonlinear behavior of beam-column connections in an RC frame and showed that the use of macro models is a suitable method for progressive collapse analysis by comparing the obtained results with experimental ones. Yi et al. (2008) investigated a 2D RC frame with four spans and three stories. During the experiment, the middle column of the lower story was removed. This experiment showed that the frame failure occurs due to the tensile rebar failure. Yu and Tan (2013) investigated the progressive collapse in an RC frame by testing two samples (one vibrational and one non-vibrational) based on the ALP method. In this way, they studied the effect of vibrational design on the frame behavior under progressive collapse. Sasani et al. (2007) investigated the behavior of a 9-story RC frame subjected to progressive collapse and concluded that the Vierendeel frame action is the dominant mechanism in load redistribution and that the greater flexural rebar strength results in greater progressive collapse resistance.

The present study investigated progressive collapse in an RC frame to examine the critical effects of removing a vertical supporting element on the response of an RC structure. As a result, a numerical model was developed in ABAQUS (2012) to perform nonlinear analysis of the RC frame behavior under a progressive collapse. Results of an experimental study given in the literature were compared to those of the present study to ensure the accuracy of numerical results.

2. Finite Element Modeling

In this study, experimental results given by Sagiroglu (2012) were used to model progressive collapse mechanism and evaluate the accuracy of the finite element model. The specifications of the RC frame and mechanical properties of the concrete and steel materials were considered to be the same as those of the experimental study. The structure was designed in compliance with ACI. The concrete damaged plasticity model was used to define the concrete. In this model, cracking occurs when tensile stresses exceed the tensile strength of concrete. The stress-strain curve of the concrete in the compressive area was developed by the experimental study (Sagiroglu, 2012). The compressive strength of the concrete was equal to 25 MPa. The tensile strength of the concrete was considered to be $0.62\sqrt{f_c'}$, where f_c' is the compressive strength of the concrete. The tensile stress-strain curve of the concrete was drawn based on the model proposed by Hillerborg (Kwak and Filippou, 1990). The stress-strain equation of the concrete was considered according to the curve in Fig. 2(a).

The following properties for the steel material were used in the modeling: density of 7860 kg/m^3 modulus of elasticity of 2.1x10^5 N/mm^2, Poisson's ratio of 0.3, yield stress of 380 MPa, and ultimate stress of 530 MPa. The stress-strain curve of the steel materials was considered bilinear with strain hardening in the plastic area. Figure 2B represents the stress-strain curve of steel material. In the modeling, a 3D 8-node element type that uses the integration by reduction formula to solve the integrations was selected for modeling the concrete elements, while 3D 2-node element type was used for modeling longitudinal and transversal rebars, which were embedded in the concrete (ABAQUS, 2012).

According to GSA (2003), a dead load plus 25% live load were introduced to the beams. The dead load, live load, and load from surrounding walls were considered to be 690 kN/m^2, 482 kN/m^2 and 690 kN/m^2, respectively. Meshing was carried out through the regular meshing technique. The mesh size was selected in a way

that the analysis results became relatively independent of the grid. In addition, the analysis speed was considered in the determination of grid size. To remove the column in the dynamic stage, the *Remove Element was used and the middle column of the first story was removed in 0.002 seconds.

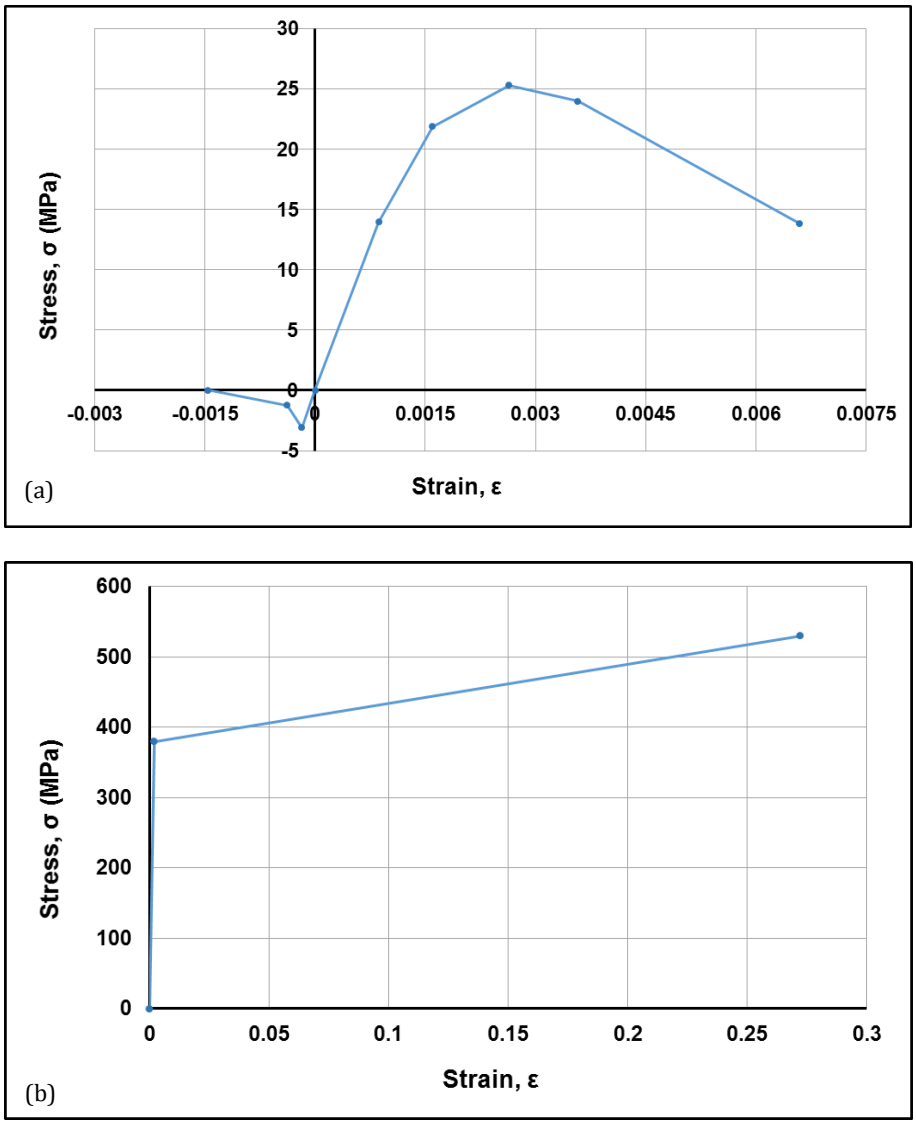

Fig. 2. (a) Concrete stress-strain curve for concrete damaged plasticity model; (b) Stress-strain curve of steel.

3. Details of the Investigated Model

In this study, an RC frame with three stories and four spans was considered as provided by Sagiroglu (2012). To meet the instantaneous column removal conditions in Sagiroglu's experiment (2012), the middle column of the first story was built with glass. In this way, the RC frame resistance to progressive collapse could be investigated with sudden smash of this glass column. Fig. 3 presents the investigated RC frame. This experimental test was carried out in two stages. In the first stage (dynamic stage), the static load was introduced to the beams and the dynamic behavior of the structure after sudden removal of the column was evaluated. Fig. 4 presents the mechanism of loading at this stage. The beam weight was considered as its dead load without applying other loads.

In the second stage (static stage), the load introduced to the beams in the first stage was eliminated, and a linear incremental displacement along the column was removed and introduced to the roof level. In this way, the performance of RC frame subjected to progressive collapse was evaluated. Fig. 5(a) shows dimensional properties and details of the beam and column reinforcement in the first and second stories. Fig. 5(b) depicts dimensional properties and details of the beam and column reinforcement in the third story. The beam has been subjected to uniformly distributed loads. To simulate the boundary conditions, all columns were fixed on the ground. To this end, all transitional and rotational degrees of freedom in finite element software was supposed to be zero. Fig. 6 presents the developed model with its loading and boundary conditions.

Fig. 3. RC frame tested by Sagiroglu (2012).

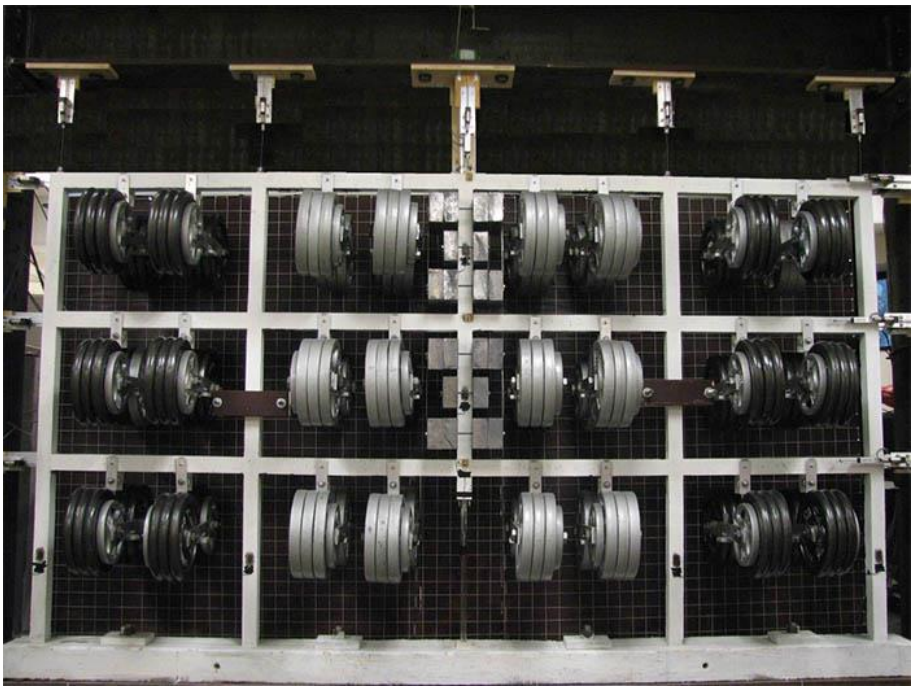

Fig. 4. Mechanism of static loading in Sagiroglu's experiment (2012).

4. Comparison of Results from Numerical Modeling and Experimental Study

The history of vertical displacement at the roof level was obtained along the removed column and presented in Fig. 7. According to experimental results, there is a peak vertical displacement of 10.6 mm during, the vibration, and a permanent displacement of 9.9 mm after approximately 1.25 seconds. According to the numerical results, there is a peak vertical displacement of 11.5 mm during the vibration, and a permanent displacement of 10.4 mm at the end of vibration. The difference between experimental and numerical results based on the permanent displacement after vibration was approximately 5%. Therefore, it can be said that the finite element modeling results are well consistent with experimental data.

In the second stage, with the introduction of linear incremental loading, the middle column at the roof level was displaced downward by 412 mm. Fig. 8 presents the frame deformation in the ultimate displacement during the experiment. Fig. 9 presents the frame deformation in the finite element model during the experiment. A good agreement was observed between the experimental and numerical results in terms of the mechanism of RC frame failure and the location of plastic hinge formation.

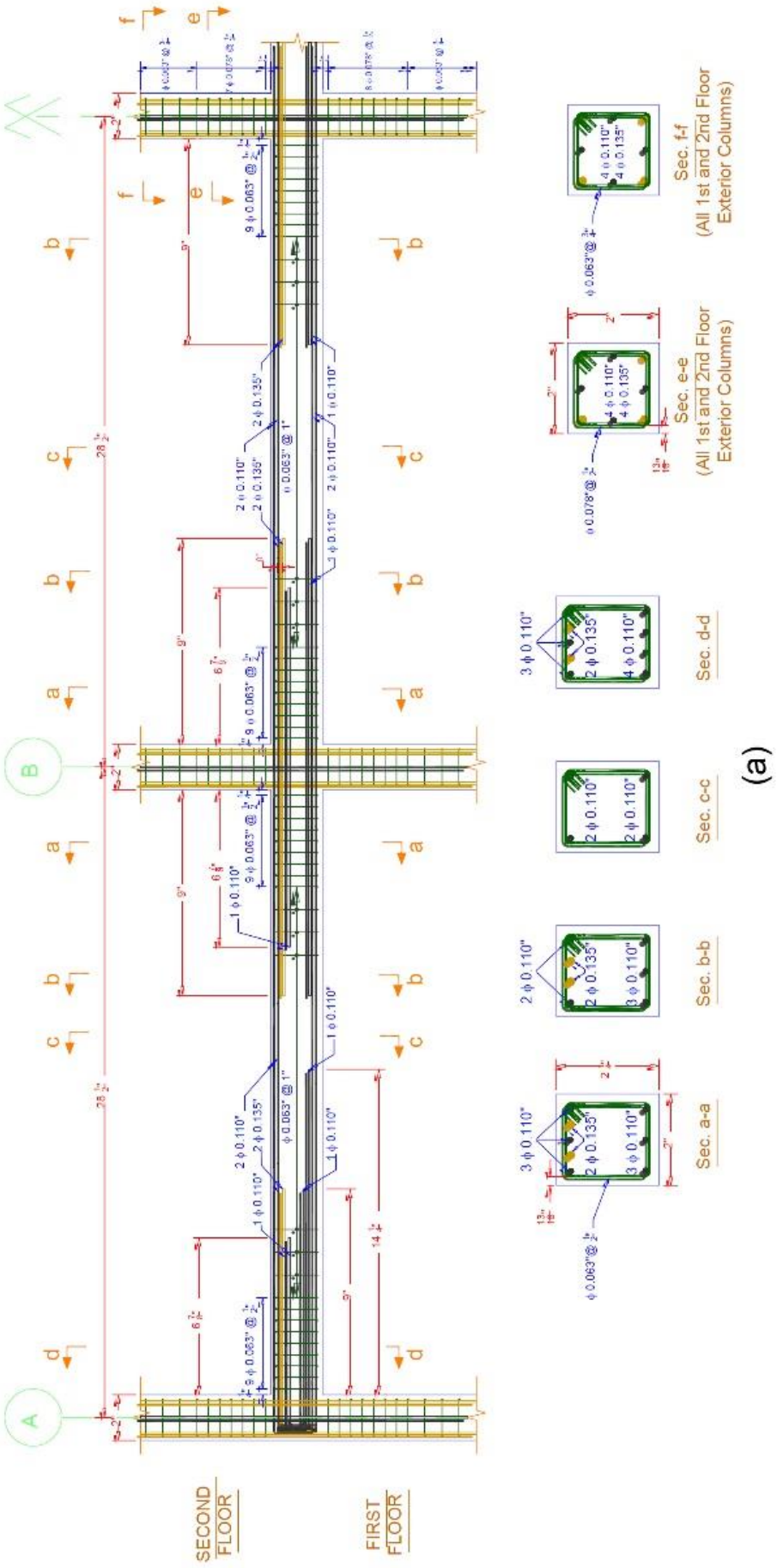

Fig. 5. (continued)

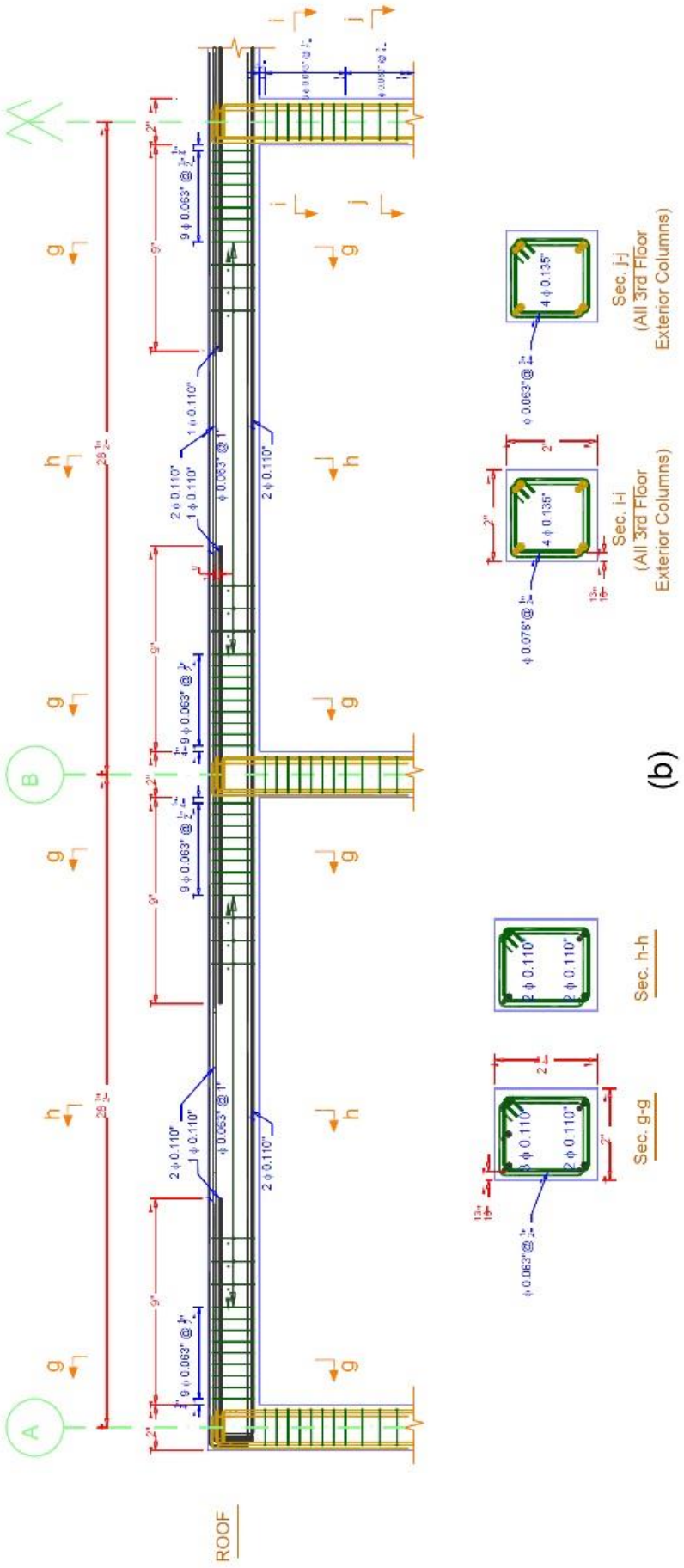

Fig. 5. Details of frame reinforcement in the experimental (Sagiroglu, 2012) and numerical studies: (a) First and second floor; (b) Third floor.

Fig. 10 presents the experimental and numerical results pertaining to vertical load changes based on vertical displacement of the middle column in the second stage of the experiment. At this stage, the resisting force increased to 8.1 kN and the beam bending failure took place due to the flexural strength of beams at both sides of the middle span. After the bending failure of the beams, the resisting force increased gradually and slightly and reached its peak level (8.81 kN) at vertical displacement of 119mm. After this stage, a sudden reduction was observed in the resisting force with formation of the plastic hinge in the beam. This reduction was up to 5.89 kN for vertical displacement of 228mm. After the formation of plastic hinge in the beams, the resisting force increased again, because of the catenary action, and finally increased to 9.42 kN for the peak vertical displacement of 412 mm. Accordingly, there is a good consistency between the results from finite element modeling and experimental data.

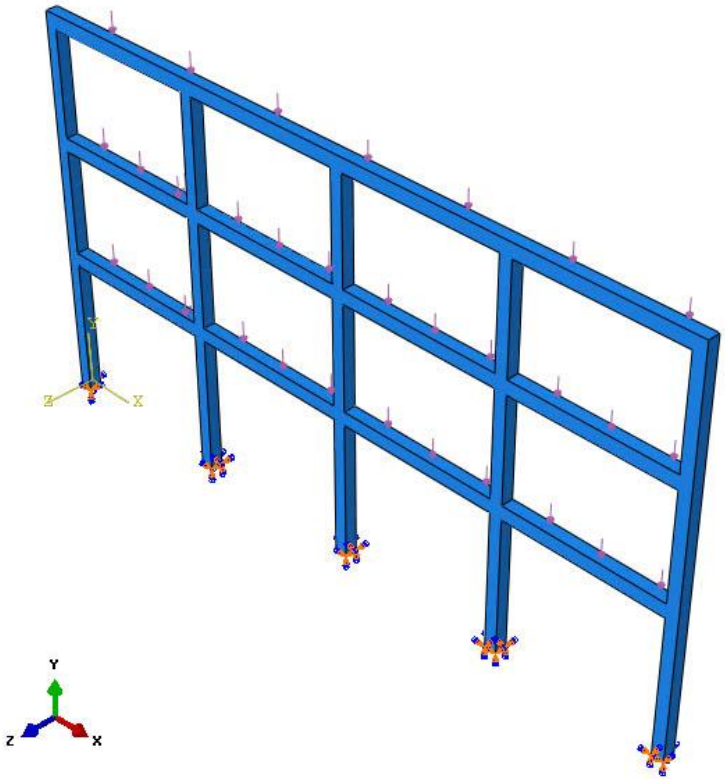

Fig. 6. Developed model with loading and boundary conditions.

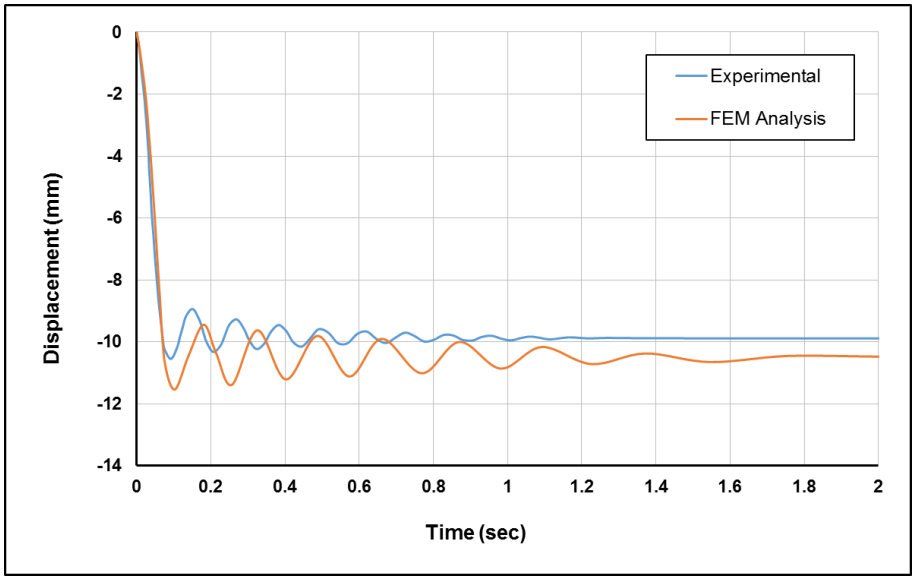

Fig. 7. Vertical displacement at the floor level of the middle column in the dynamic stage.

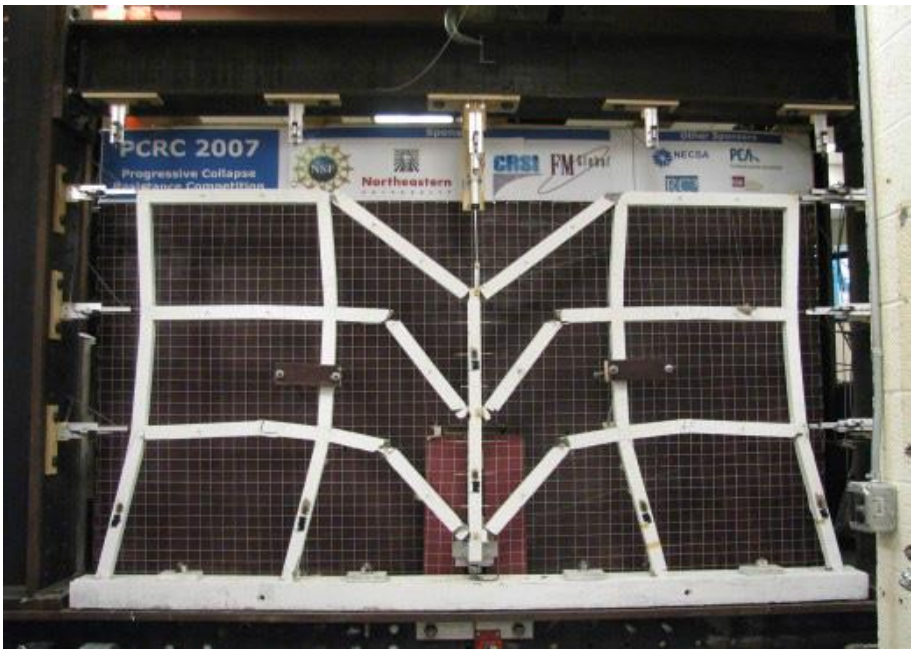

Fig. 8. Deformed frame in the experimental study (Sagiroglu, 2012).

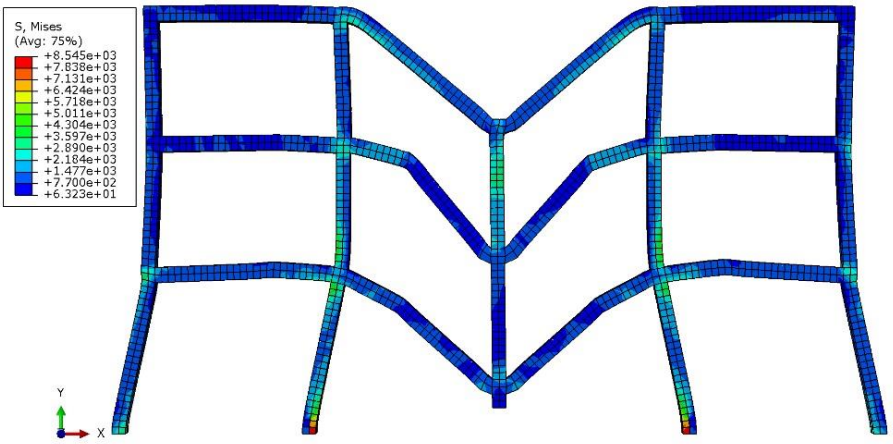

Fig. 9. Deformed frame in the finite element model.

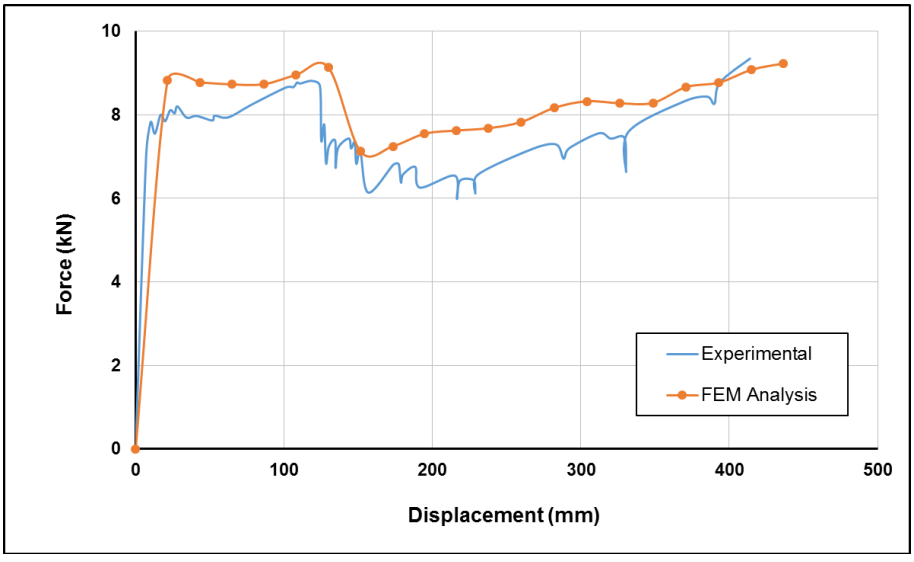

Fig. 10. Changes of resisting force-vertical displacement at middle column in static stage.

5. Conclusions

It is essential in numerical studies to ensure the accuracy of modeling results to turn the model into a reliable basis for future studies. Comparison of experimental and numerical results is a way to achieve this goal. As a result, similar experimental results were used to validate the numerical modeling solutions. Specifically, in the study of the behavior of concrete elements, the behavioral complexity of concrete materials, along with the combined function of concrete and steel materials, necessitates a method for validation of numerical analysis. With respect to progressive collapse of RC structures, the lack of adequate experimental results and high cost of experimental studies highlight the need for a reliable numerical model. In this study, a numerical model was developed for nonlinear analysis of the behavior of an RC frame subjected to progressive collapse. Comparison between the results of numerical analysis and those of the experiments on the investigated RC frame indicated a good agreement, suggesting an acceptable accuracy of the modeling. Investigating the effect of the third dimension elements, the effect of infill panel walls, the position of the removed column, etc. can be considered to be a basis for future studies on progressive collapse in RC structures. As a result, the proposed model can be used for conducting more relevant studies by keeping the modeling parameters constant.

References

ABAQUS version 6.12 (2012). Hibbitt, Karlsson & Sorensen Inc., Pawtucket, Rhode Island, USA.

ACI 318 (2014). Building Code Requirements for Structural Concrete. American Concrete Institute, Farmington Hills, Michigan, USA.

ASCE 7-16 (2016). Minimum design loads for buildings and other structures. American Society of Civil Engineers, Reston, Virginia, USA.

Bao Y (2008). Macro model based progressive collapse simulation of reinforced concrete structures. *Ph.D thesis*, University of California, Davis, USA.

Bažant ZP, Verdure M (2007). Mechanics of progressive collapse: learning from World Trade Center and building demolitions. ASCE Journal of Engineering Mechanics, 133(3), 308-319.

Corley WG, Mlakar PF, Sozen MA, Thornton CH (1998). The Oklahoma City bombing: Summary and recommendations for multihazard mitigation. *Journal of Performance of Constructed Facilities*, 12(3), 100-112.

DoD (2009). Design of Buildings to Resist Progressive Collapse. Department of Defense, UFC, 4-023-03, Washington DC, USA.

GSA (2003). Progressive collapse analysis and design guidelines for new federal office buildings and major modernization projects. The US General Services Administration, Washington DC, USA.

Iwankiew N, Griffis L (2004). Comparison of structural performance of multi-story buildings under extreme events. American Institute of Steel Construction, Chicago, Illinois, USA.

Kaewkulchai G, Williamson E (2003). Dynamic behavior of planar frames during progressive collapse. *16th ASCE Engineering Mechanics Conference*, University of Washington, Seattle, 1-12.

Kwak HG, Filippou FC (1990). Finite element analysis of reinforced concrete structures under monotonic Loads. Department of Civil Engineering, University of California, Berkeley, California, USA.

NBCC (2005). National Research Council of Canada. National Building Code of Canada, Ottawa, Ontario, Canada.

Pearson C, Delatte N (2003). Lessons from the progressive collapse of the Ronan Point Apartment Tower. *Proceedings of the 3rd ASCE Forensics Congress*, San Diego, California, United States, 190-200.

Reeve S (1999). The new jackals: Ramzi Yousef, Osama Bin Laden and the future of terrorism. Northeastern University Press, Boston, MA.

Ruth P, Marchand KA, Williamson EB (2006). Static equivalency in progressive collapse alternative path analysis: Reducing conservatism while retaining structural integrity. *Journal of Performance of Constructed Facilities*, 20(4), 349-364.

Sagiroglu S (2012). Analytical and experimental evaluation of progressive collapse resistance of reinforced concrete structures. *Ph.D thesis*, Northeastern University, Boston, Massachusetts, USA.

Sasani M, Bazan M, Sagiroglu S (2007). Experimental and analytical progressive collapse evaluation of actual reinforced concrete structure. *ACI Structural Journal*, 55(6), 731-739.

Starossek U (2009). Progressive Collapse of Structures. Thomas Telford Ltd., London, UK.

Yi WJ, He QF, Xiao Y, Kunnath SK (2008). Experimental study on progressive collapse-resistant behavior of reinforced concrete frame structures. *ACI Structural Journal*, 105(4), 433-439.

Yu J, Tan KH (2013). Experimental investigation on progressive collapse resistance of reinforced concrete beam column sub-assemblages. *Engineering Structures Journal,* 55(1), 90-106.